1 Cloud response to co-condensation of water and organic vapors over the boreal
2 forest

4 Liine Heikkinen[1,2], Daniel G. Partridge[3], Wei Huang[4], Sara Blichner[1,2], Rahul Ranjan[1,2],
5 Emanuele Tovazzi[3], Tuukka Petäjä[4], Claudia Mohr[1,2], and Ilona Riipinen[1,2]

6 [1]Department of Environmental Science (ACES), Stockholm University, Stockholm, Sweden
7 [2]Bolin Centre for Climate Research, Stockholm University, Stockholm, Sweden
8 [3]Department of Mathematics and Statistics, Faculty of Environment, Science and Economy, University of Exeter,
9 Exeter, United Kingdom
10 [4]Institute for Atmospheric and Earth System Research (INAR) / Physics, University of Helsinki, Helsinki, Finland
11
12 *Correspondence to*: Liine Heikkinen (liine.heikkinen@aces.su.se) and Ilona Riipinen (ilona.riipinen@aces.su.se)

13 **Abstract**

14 Accounting for the condensation of organic vapors along with water vapor (co-condensation) has been shown in
15 adiabatic cloud parcel model (CPM) simulations to enhance the number of aerosol particles that activate to form
16 cloud droplets. The boreal forest is an important source of biogenic organic vapors, but the role of these vapors in
17 co-condensation has not been systematically investigated. In this work, the environmental conditions under which
18 strong co-condensation -driven cloud droplet number enhancements would be expected over the boreal biome are
19 identified. Recent measurement technology, specifically the Filter Inlet for Gases and AEROsols (FIGAERO)
20 coupled to an iodide-adduct Chemical Ionization Mass Spectrometer (I-CIMS), is utilized to construct a volatility
21 distribution of the boreal atmospheric organics. Then, a suite of CPM simulations initialized with a comprehensive
22 set of concurrent aerosol observations collected in the boreal forest of Finland during Spring 2014 is performed.
23 The degree to which co-condensation impacts droplet formation in the model is shown to be dependent on the
24 initialization of the updraft velocity, aerosol size distribution, organic vapor concentration and the volatility
25 distribution. The predicted median enhancement in cloud droplet number concentration (CDNC) due to
26 accounting for the co-condensation of water and organics is 20% (interquartile range 29–14%). This corresponds
27 to activating particles 12–16 nm smaller in dry diameter, that would otherwise remain as interstitial aerosol. The
28 highest CDNC enhancements (ΔCDNC) are predicted in the presence of a nascent ultrafine aerosol mode with a
29 geometric mean diameter of ~40 nm and no clear Hoppel minimum, indicative of pristine environments with a
30 source of ultrafine particles (e.g., via new particle formation processes). Such aerosol size distributions are
31 observed 30–40% of the time in the studied boreal forest environment in spring and fall when new particle
32 formation frequency is the highest (six years of statistics). Five years of UK Earth System Model (UKESM1)
33 simulations are further used to evaluate the frequencies to which such distributions are experienced by an Earth
34 System Model over the whole boreal biome. The frequencies are substantially lower than those observed at the
35 boreal forest measurement site (<6% of the time) and the positive values, peaking in spring, are modeled only
36 over Fennoscandia and western parts of Siberia. For the aerosol size distribution regime simulated by UKESM1,
37 offline simulations with the adiabatic parcel model reveal the ΔCDNC to be sensitive to the concentrations of
38 semi-volatile and some intermediate-volatility organic compounds (SVOCs and IVOCs). The magnitudes of
39 ΔCDNC remain less affected by the more volatile vapors such as formic acid and extremely low and low volatility
40 organic compounds (ELVOCs and LVOCs) in the CPM simulations. The reasons for this are that most volatile
41 organic vapors condense inefficiently due to their high volatility below cloud base and the concentrations of
42 LVOCs and ELVOCs are too low to gain significant concentrations of soluble mass to reduce critical

43 supersaturations needed for droplet activation. Suppression of the critical supersaturation caused by organic

44 condensation is the main driver of the modeled ΔCDNC. The results highlight the potential significance of co-

45 condensation in pristine boreal environments close to sources of fresh ultrafine particles. For accurate predictions

46 of co-condensation effects on CDNC, the representation of the aerosol size distribution is of essence. Further

47 studies targeted at finding observational evidence and constraints for co-condensation in the field are encouraged.

48

49 **1 Introduction**

50 Boreal forests emit significant quantities of volatile organic compounds (VOCs, Guenther et al., 1995; Artaxo et

51 al., 2022), such as monoterpenes, that undergo oxidation in the atmosphere. The condensable oxidation products

52 contribute considerably to the secondary organic aerosol (SOA) mass concentrations in the boreal forest air (e.g.,

53 Tunved et al., 2006; Artaxo et al., 2022). The emissions of monoterpenes are strongly temperature-dependent,

54 which leads – together with the higher oxidative potential in the sunlit months – to highest biogenic SOA

55 concentrations in summer (Paasonen et al., 2013; Heikkinen et al., 2020; Mikhailov et al., 2017). This has recently

56 been shown to have implications for cloud properties above the boreal forest through the availability of more

57 cloud condensation nuclei (CCN; Yli-Juuti et al., 2021; Petäjä et al., 2022). Under constant meteorological

58 conditions, an increase in aerosol concentration typically results in an increase in CDNC and smaller average

59 droplet size for a given liquid water content (Yli-Juuti et al., 2021). These effects alter the cloud brightness making

60 clouds scatter incoming solar radiation more efficiently (Twomey effect; Twomey, 1974, 1977). The relationships

61 between the number of aerosol particles, cloud droplet number concentration (CDNC), and their effects on climate

62 are non-linear and complex, which makes aerosol-cloud interactions the largest source of uncertainty in radiative

63 forcing estimates from climate models (e.g., Lohmann and Feichter, 2005; Carslaw et al., 2013; Bellouin et al.,

64 2020). The development of "bottom-up" predictive models is needed for providing accurate, yet robust,

65 simplifications of key processes involved in aerosol-cloud interactions – eventually for inclusion in climate

66 models in computationally efficient parameterizations.

67 Numerous studies have been carried out to understand the role of condensable organic vapors in SOA

68 formation (e.g., Hallquist et al., 2009; Shrivastava et al., 2017) and hence the concentrations of CCN (i.e. particles

69 of at least 50–100 nm in diameter for the water vapor supersaturations typical of the boreal environments; Cerully

70 et al., 2011; Sihto et al., 2011; Paramonov et al., 2013; Hong et al., 2014; Paramonov et al., 2015). The yields of

71 volatile, intermediate-volatility or semi-volatile organic compounds (VOCs, IVOCs, or SVOCs) from

72 monoterpene oxidation, such as those of pinonaldehyde, formic acid, or acetic acid, are generally much higher

73 than those of the readily condensable lower-volatility vapors (low-volatility organic compounds, LVOCs and

74 extremely low volatility organic compounds, ELVOCs). The above-mentioned volatility classes are determined

75 based on the volatilities of individual compounds binned into a volatility basis set (VBS; Donahue et al., 2006):

76 VOCs have a saturation vapor concentration (C^*; given in units of μg m^{-3} throughout the paper) of at least 10^7 μg

77 m^{-3}, IVOCs are distributed in the C^* range of $[10^3, 10^6]$ μg m^{-3}, SVOCs of $[1, 100]$, LVOCs of $[10^{-3}, 10^{-1}]$ and

78 ELVOCs have a C^* below 10^{-4} μg m^{-3} (e.g., Donahue et al., 2011). While VOCs, IVOCs, and some SVOCs are

79 unlikely to produce significant concentrations of SOA at ground level without additional oxidation steps or

80 reactive uptake, some of them can condense at higher altitudes if transported aloft (e.g., Murphy et al., 2015). This

81   work focuses on the role of SVOCs and IVOCs in warm cloud microphysics due to their high abundance in
82   tropospheric air and co-condensation potential.

83   Warm (liquid) clouds can form when air rises and cools, eventually leading to the air being supersaturated
84   with water vapor. The excess water vapor condenses onto aerosol particles, rapidly growing them into cloud
85   droplets. While water vapor represents the most abundant vapor in the atmosphere, also other trace species can
86   influence the cloud droplet activation process as the cooling of the rising air triggers also their condensation. As
87   the trace vapors condense, the molar fraction of water in the swelling droplets increases slower than in the absence
88   of co-condensation, which in turn leads to the condensation of additional water by the time the air parcel reaches
89   lifting condensation level. The co-condensation of water with other vapors eventually leads to a reduction in
90   critical supersaturation (s^*) required for droplet activation of the particles due to an increased amount of organic
91   solute (Topping and McFiggans, 2012) as described by Köhler theory (Köhler, 1936). Topping et al. (2013)
92   studied the impact of organic co-condensation on CDNC using a cloud parcel model (CPM) initialized with a
93   suite of realistic conditions describing the aerosol particle number size distribution (PNSD), composition, and
94   organic aerosol (OA) volatility distribution. They showed significant enhancements in CDNC (ΔCDNC up to
95   roughly 50%) when comparing simulations with organic condensation (CC) to simulations without (noCC). In
96   addition to co-condensing organics and water, also co-condensation of nitric acid and ammonia together with
97   water has been suggested to enhance CDNC in earlier process modeling studies (e.g., Kulmala et al., 1993;
98   Korhonen et al., 1996; Hegg, 2000; Romakkaniemi et al., 2005). Direct experimental studies of co-condensation
99   remain challenging, however, as aerosol particles are typically dried during the sampling process and the loss of
100   liquid water may lead to evaporation of co-condensed organics, too. While direct observational evidence of
101   organic co-condensation in the atmosphere is still lacking, recent laboratory studies show significant water uptake
102   due to co-condensation of propylene glycol and water onto ammonium sulfate particles (Hu et al., 2018).

103   The cloud response to co-condensation in the form of ΔCDNC is the result of a complex interplay
104   between updraft velocity, PNSD and organic compound volatility distribution (Topping et al., 2013). For the same
105   amount of organic vapor, Topping et al. (2013) modelled a non-linear updraft response of ΔCDNC. The highest
106   ΔCDNC were obtained when updrafts were below 1 m s^{-1}, but the peak ΔCDNC was dependent on the initial
107   PNSD characteristics. Under higher updrafts, the modelled ΔCDNC was found to decrease exponentially as a
108   function of updraft, but the asymptote of the curve depended on the initial PNSD – although the dependence on
109   the exact parameters describing multimodal PNSD were not extensively explored. If assumed representative of
110   the global continents, ΔCDNC values of tens of percent could impose a significant impact on predictions of cloud
111   albedo and the Earth's radiative budget. In fact, Topping et al. (2013) suggest accounting for co-condensation
112   could result in up to 2.5% increase in cloud albedo (corresponding to global ΔCDNC = 40%). This albedo increase
113   would translate into a –1.8 W m^{-2} change in the global cloud radiative effect over land. Topping et al. (2013)
114   stress, however, that the impacts of co-condensation will be spatially heterogeneous because of variable surface
115   albedo and variation in VOC sources. For comparison, one should note that the net radiative effect of clouds is
116   approximately –20 W m^{-2} (Boucher et al., 2013). The recent best estimate of the effective radiative forcing from
117   aerosol-cloud interactions is, on the other hand, –1.0 [–1.7 to –0.3] W m^{-2} (Forster et al., 2021). The potential
118   contribution of co-condensation to estimates on aerosol forcing or to future cloud radiative effects remains unclear.

119   Boreal forests make up about one third of the Earth's forested area, which makes it an important source
120   of biogenic vapors that could affect droplet activation in warm clouds through co-condensation. ΔCDNC due to

121 co-condensation over the boreal forest could reduce the albedo over the dark boreal forest canopy. In a warming
122 climate, temperature-dependent biogenic terpene emissions (Guenther et al., 1993) are expected to rise (e.g.,
123 Turnock et al., 2020). These increasing emissions enrich the ambient pool of organics available for condensation
124 in rising air. As suggested in Topping et al. (2013), through the effects organic co-condensation poses on CDNC,
125 co-condensation could enhance the proposed negative climate feedback mechanism associated with the biogenic
126 SOA (Kulmala et al., 2004; Spracklen et al., 2008; Kulmala et al., 2014; Yli-Juuti et al., 2021), the magnitude of
127 which is currently highly uncertain (Thornhill et al., 2021; Sporre et al., 2019; Scott et al., 2018; Paasonen et al.,
128 2013; Sporre et al., 2020).

129 Since the publication of the Topping et al. (2013) study, improved constraints of the effective volatilities
130 of organic aerosol (e.g., Thornton et al., 2020) can be placed through the application of chemical ionization mass
131 spectrometers (CIMS) providing molecular level information on gas- and particle-phase composition in near-real
132 time. With the up-to-date volatility parameterizations using the molecular formulae retrieved from CIMS data,
133 volatility distributions can be calculated along a volatility scale ranging from ELVOCs to VOCs, while previous
134 techniques could not enable constraints on volatilities exceeding $C^* = 1000$ μg m^{-3} (SVOC) (Cappa and Jimenez,
135 2010). This means that a notable amount of semi- and intermediate volatility vapors with high co-condensation
136 potential were not included in the early organic co-condensation work (Topping et al., 2013; Crooks et al., 2018).
137 The recent methodological developments motivate revisiting work of Topping et al. (2013), as potentially large
138 concentrations of condensable organic vapors have been so far neglected.

139 In this study, the cloud response to the co-condensation of organic vapors over the boreal forest of
140 Finland is investigated using a CPM. Measurements and parameterization techniques involving FIGAERO-I-
141 CIMS data are utilized to constrain the volatility distribution of organics for these simulations. In addition, to
142 ensure realistic modeling scenarios, simultaneously recorded measurements of PNSD and chemical composition
143 from the Aerosol Chemical Speciation Monitor (ACSM) are used for the CPM initialization. 97 CPM simulations
144 initialized with conditions from boreal spring and early summer following measurement time series recorded
145 during the Biogenic Aerosols – Effects on Clouds and Climate (BAECC) campaign at the Station Measuring
146 Atmosphere–Ecosystem Relationships (SMEAR) II (Hari and Kulmala, 2005) in Finland (Petäjä et al., 2016) are
147 performed, and sensitivity to updraft velocity is studied. These simulations are then used to characterize the
148 environmental conditions (with respect to the size distribution and organic aerosol volatility distribution
149 characteristics) that promote co-condensation-driven CDNC enhancements in the boreal atmosphere. The
150 frequencies to which a strong cloud response to co-condensation can be expected and its spatiotemporal variability
151 over the boreal biome is further investigated using long-term measurements from SMEAR II station and UK Earth
152 System Model (UKESM1) simulations.

2 Methods and Data

2.1 The adiabatic cloud parcel model (ICPM)

155 The CPM chosen for this study is the Institute for Marine and Atmospheric research Utrecht (IMAU) entrained
156 pseudo-adiabatic CPM (ICPM, Roelofs and Jongen, 2004). ICPM was further developed so that it could perform
157 simulation of both pseudo-adiabatic and adiabatic ascents of air parcels (Partridge et al., 2011, 2012). ICPM
158 simulates the condensation and evaporation of water vapor on aerosol particles, particle activation to cloud
159 droplet, unstable growth, collision and coalescence between droplets, and aqueous phase sulphur chemistry.

160   The model can be initialized with aerosol populations consisting of one or more internal or external
161   mixtures of sulfuric acid, ammonium bisulfate, ammonium sulfate, OA, black carbon, mineral dust and sea salt.
162   The PNSD are presented in a moving-center binned microphysics scheme comprising 400 size bins between 5 nm
163   and 5 μm in dry radii, which are constructed at model initialization from the three parameters describing log-
164   normal size distributions for the i number of modes – the geometric mean diameter (D_i), the total mode number
165   concentration (N_i), and the geometric standard deviation (σ_i). The model can be initialized with up to four log-
166   normal aerosol modes. The ICPM further provides time evolutions of key thermodynamic and microphysical
167   parameters e.g., the air parcel temperature (T), pressure (p), supersaturation (s), altitude (z) and the aerosol particle
168   and hydrometeor size distributions.

169   The dynamical equations used in the ICPM to simulate the adiabatic ascending air parcel equations are
170   same to those presented by Lee and Pruppacher (1977), where the vertical parcel displacements are determined
171   by the updraft velocity (w, set to a fixed positive constant value in the ICPM simulations):

$$\frac{\mathrm{d}z}{\mathrm{d}t} = w. \tag{1}$$

172   The changes in pressure are calculated assuming hydrostatic balance and the temperature decrease along the ascent
173   follows the dry adiabatic lapse rate while also accounting for the latent heat release due to condensation:

$$-\frac{\mathrm{d}T}{\mathrm{d}t} = \frac{gw}{c_{p,a}} + \frac{L_e}{c_{p,a}}\frac{\mathrm{d}x_v}{\mathrm{d}t} + \mu_J\left[\frac{L_e}{c_{p,a}}(x_v - x_v') + (T - T')\right]w \tag{2}$$

174   where g is the acceleration of gravity, L_e the latent heat of evaporation, $c_{p,a}$ the specific heat capacity of air and x_v
175   the water vapor mixing ratio of the air parcel. μ_J is the entrainment rate describing mixing of parcel air with
176   environmental air characterized with x_v' and T'. In this study, in which adiabatic simulations are performed,
177   entrainment is not considered ($\mu_J = 0$). The water vapor mixing ratio in the air parcel changes with the evolving
178   ambient supersaturation:

$$\frac{\mathrm{d}s}{\mathrm{d}t} = \frac{p}{\varepsilon e_s}\frac{\mathrm{d}x_v}{\mathrm{d}t} - (1+s)\left[\frac{\varepsilon L_e}{R_a T^2}\frac{\mathrm{d}T}{\mathrm{d}t} + \frac{g}{R_a T}w\right], \tag{3}$$

179   where $\varepsilon = R_a/R_v = M_w/M_a = 0.622$ i.e., the ratio between the specific gas constants for air and water vapor or
180   alternatively the molecular weight of water and air. e_s is the saturation vapor pressure of water. To solve the
181   ordinary differential equations (Eqs. 2–3), the time derivate of the water vapor mixing is approximated as

$$\frac{\mathrm{d}x_v}{\mathrm{d}t} \approx -\frac{\Delta x_L}{\Delta t} - \mu_J(x_v - x_v' + x_L)w \tag{4}$$

182   where Δt is the model time step (10^{-3} seconds) and the liquid water mixing ratio (x_L) is calculated as a sum of the
183   liquid water mixing ratio across all the 400 size bins (index i) for each assigned mode composition (index j):

$$\Delta x_L = \frac{4\pi\rho_w}{3\rho_a}\sum_{i=1}^{n_a}\sum_{j=1}^{n_b}n_{ij}\left(r_{ij}^3 - r_{ij,\mathrm{dry}}^3\right), \tag{5}$$

184   where ρ_w is density of water, ρ_a is the density of the particle dry mass, n_{ij} is the number of particles within size bin
185   i and composition j, and finally r_{ij} and $r_{ij,\mathrm{dry}}$ are the wet and dry radii of the particles, respectively. The wet radii
186   and hence also the particle masses (m) change as water condenses onto the particle (indices dropped for
187   simplicity):

$$\frac{\mathrm{d}m}{\mathrm{d}t} = 4\pi\rho_w r^2 \frac{\mathrm{d}r}{\mathrm{d}t} = \frac{4\pi\rho_w r\,(S-S_{\mathrm{eq}})}{\frac{\rho_w RT}{\mathrm{DIFF}_v^* e_s} + \frac{L_e\rho_w}{kT}\left(\frac{L_e}{RT}-1\right)}, \tag{6}$$

188   where k is the thermal conductivity, and DIFF_v^* is size-dependent water vapor diffusivity (from Pruppacher and

189   Klett, 1997). Eq. (6) is approximated within the ICPM using a linearized form of the condensation equation

190   (Hänel, 1987). Finally, S is the ambient saturation ratio ($S = s + 1$) and S_{eq} ($S_{\mathrm{eq}} = \mathrm{RH} / 100\%$) the equilibrium

191   saturation ratio over the (spherical) wet particle surface, the difference of which determines the quantity of excess

192   vapor for the diffusional growth of the particle. While S depends on the updraft source and condensation sink (Eq.

193   3), S_{eq} depends on the particle wet radius and composition and it can be calculated using the Köhler equation

194   (Köhler, 1936), traditionally expressed as:

$$S_{\mathrm{eq}} = \frac{e}{e_s} = a_w \exp\left(\frac{2M_w\gamma}{RT\rho_w r}\right) \tag{7}$$

195   where e is the vapor pressure of water, a_w the water activity, γ the droplet surface tension (assumed to be that of

196   water; see Table 1), R the universal gas constant, T the droplet temperature and r the droplet radius. Assuming

197   dilute droplets, Eq. 7 is approximated in ICPM as follows for the equilibrium supersaturation ratio (Hänel, 1987):

$$S_{\mathrm{eq}} \approx \exp\left(\frac{A}{r} - \frac{B}{\left(\frac{r}{r_{\mathrm{dry}}}\right)^3 - 1}\right), \tag{8}$$

198   where

$$A = \frac{2M_w\gamma}{RT\rho_w} \tag{9}$$

199   and

$$B = \frac{3n_s M_w}{4\pi\rho_w}. \tag{10}$$

200   A and B in Eqs. (9) and (10) are the Köhler coefficients, where n_s is the total number of solutes (mol). The Raoult

201   term (Eq. 10) is reformulated within the ICPM in terms of solute concentrations enabling its adjustments by

202   dissolving or partially dissolving chemical constituents. For detailed descriptions of the B term, the reader is

203   directed to Roelofs (1992).

204

205   **2.1.1 Gas–particle partitioning of organics**

206   ICPM has been extended to incorporate Köhler and condensation/evaporation equations for organic species of

207   varying volatilities (Lowe, 2020). The volatility distributions are given using the VBS framework (Donahue et

208   al., 2006). Initially, each volatility bin q contains the sum of gas ($C_{g,q}$) and particle phase concentrations ($C_{p,q}$;

209    $C_{g+p,q} = C_{g,q} + C_{p,q}$) of the compounds with a given C^*. The partitioning coefficients for each bin, ξ_q, are defined

210   as

$$\xi_q \equiv \frac{C_{p,q}}{C_{p,q} + C_{g,q}}. \tag{11}$$

211   The total particle phase mass concentration across all volatility bins is

$$C_p = \sum_q C_{p,q} = \sum_q C_{g+p,q}\,\xi_q \tag{12}$$

212 and the partitioning coefficients depend on C^* as follows

$$\xi_q = \frac{C_p}{C_p + C_q^*}. \tag{13}$$

213 ξ_q are solved iteratively from Equations (12–13) at model initialization. Similarly, as in the work of Topping et

214 al. (2013), C_p is constrained using the initial PNSD and the organic mass fraction in addition to the relative

215 proportions of the various volatility bins (volatility distribution shape).

216 The condensation/evaporation equation for organic species is described in the same manner as in Topping

217 et al. (2013) and as shown for water vapor in Eq (6):

$$\frac{dm_q}{dt} = \frac{4\pi \rho_w r \, \mathrm{DIFF}_g^* \left(S_q - S_{eq,\,q}\right) e_{s,\,q}}{\frac{\mathrm{DIFF}_g^* H_q S_{eq,\,q}\, e_s \rho_w}{kT}\left(\frac{H_q M_q}{RT}-1\right)+\frac{\rho_w RT}{M_w}} \tag{14}$$

218 where DIFF_g^* is the gas phase diffusivity (see details in Topping et al., 2013 supplementary information), H_q the

219 enthalpy of vaporization, $e_{s,\,q}$ the saturation vapor pressure, and $S_{eq,\,q}$ the equilibrium saturation ratio of organic

220 species in the qth volatility bin. $S_{eq,\,q}$ is calculated following the Köhler equation (Eq. 8) analogy:

$$S_{eq,\,q} = a_q \exp\left(\frac{2v_q \gamma}{RTr}\right) \tag{15}$$

221 where a_q is the activity of $C_{p,\,q}$ in the bulk condensed phase, which equals the molar fraction of $C_{p,\,q}$ due to the

222 ideal solution approach of the study. In the model simulations enabling organic phase transitions, the

223 concentrations of the gas and particle phases integrated over all the volatility bins are saved as model output.

224

2.2 Measurement data from SMEAR II used for ICPM initialization

226 The observational data used for the ICPM initialization were collected during the Biogenic Aerosols – Effects on

227 Clouds and Climate (BAECC) campaign which took place in 2014 at the Station Measuring Ecosystem–

228 Atmosphere Relationships (SMEAR) II in Hyytiälä, Finland (Petäjä et al., 2016). SMEAR II is a well

229 characterized atmospheric measurement supersite located within a boreal forest in Southern Finland (61°51'N,

230 24°17'E; Hari and Kulmala, 2005). The surroundings of the measurement site are mostly forested (80% within a

231 5 km radius and 65% within a 50 km radius; Williams et al., 2011). The atmospheric composition measured at the

232 site suggests strong influence of biogenic emissions on aerosol and aerosol precursor (i.e., biogenic VOCs,

233 BVOCs) concentrations (e.g., Hakola et al., 2012; Yan et al., 2016; Allan et al., 2006; Heikkinen et al., 2021).

234 Anthropogenic influence is pronounced when air masses arrive from heavily industrialized areas such as St

235 Petersburg, Russia (Kulmala et al., 2000).

236 The PNSD for the ICPM initialization are obtained from the Differential Mobility Particle Sizer (DMPS)

237 measurements from SMEAR II performed within the forest canopy (Aalto et al., 2001; Petäjä et al., 2016). Since

238 ICPM takes in the log-normal parameters that the size distribution comprises (N, D, σ), also the fitting of the

239 PNSD is performed. This is done using the Hussein et al. (2005) algorithm that allows fitting 1–4 modes into the

240 measured distributions and decides the optimal number of modes. For the BAECC data set, the optimal number

241 would always be between three and four modes, with a higher number of modes generally yielding a better fit to

242 the observational data as expected. Despite the optimal number of 3–4 modes, the maximum number of modes is

243 restricted to two as the agreement between the fitted and measured distributions remained good considering the

244 experimental uncertainties, and including two modes only instead of four considerably sped up the simulations.

245   Moreover, the DMPS is suitable for sampling aerosol particles of ca. 3–1000 nm in size (electrical mobility

246   equivalent diameter) and hence does not capture the coarse mode. In addition, the Aitken mode at SMEAR II

247   typically originates from a growing nucleation mode. In more polluted environments, where small particles have

248   sources other than new particle formation, simplifications like this might not be appropriate. The PNSD time

249   series measured during BAECC is shown in Fig. 1a. It shows clearly the growth of nucleation mode to Aitken

250   mode on several occasions. Statistics regarding the log-normal parameters of the fitted data during BAECC are

251   provided in Table 1. The bimodal fits are also calculated for the years 2012–2017. These data are used later to

252   evaluate the frequency of times size distributions yielding high ΔCDNC appear in long-term data.

253   The aerosol chemical composition for ICPM initialization are obtained from Aerosol Chemical

254   Speciation Monitor (ACSM; Ng et al., 2011) measurements performed within the forest canopy (Heikkinen et al.,

255   2020). The ACSM measures the non-refractory (NR) sub–micrometer particular matter (PM$_1$) chemical

256   composition, which means that the reported composition is restricted to organics, sulfate, nitrate, chloride and

257   ammonium. The salts measured by the instrument do not include sea salt, because it typically exists in the coarse

258   mode and does not fully evaporate at the ACSM vaporizer temperature of 600°C. The latter reason restricts the

259   instrument also from detecting black carbon (BC). The composition from the ACSM measurements is shown in

260   Fig. 1b. Statistics regarding the organic mass fractions (f_{Org}) are shown in Table 2. The ACSM data are further

261   used to derive volatility distributions similar to those utilized by Topping et al. (2013; see Sect. 2.3.1 for details).

262   An iodide FIGAERO-I-CIMS, sampling above the forest canopy in a ca. 30 m tower, is used to retrieve

263   molecular composition and volatility distributions of gas- and particle-phase species during BAECC (Mohr et al.,

264   2017, 2019; Schobesberger et al., 2016; Lee et al., 2018, 2020; see Sect. 2.3.2 for details). The Filter Inlet for

265   Gases and AEROsols (FIGAERO; Lopez-Hilfiker et al., 2014) coupled with a CIMS (the coupling of these

266   instruments hereafter referred to as FIGAERO-I-CIMS) stands as one of the very few instruments capable of

267   performing near-simultaneous measurements of both gas and particle phases. The FIGAERO inlet allows the gas

268   phase to be sampled while aerosol particles are collected on a Teflon filter, and after sufficient particle deposition

269   time the sample is heated and the evaporated molecules are measured similarly to the gas phase. The heating

270   procedure, which typically reaches a maximum temperature of around 200°C can, however, cause thermal

271   fragmentation of molecules (Lopez-Hilfiker et al., 2015). This leads to the detection of small molecular fragments,

272   which get assigned a higher C^* than that of the parent molecule, which can be seen in the FIGAERO-I-CIMS

273   thermograms when compounds with high C^* vaporize at exceptionally high temperatures. In addition to the

274   indistinguishable isomers from any of the phases from online FIGAERO-I-CIMS measurements (or any other

275   mass spectrometer for that matter), thermal fragmentations add to the uncertainty of volatility distributions

276   retrieved from these data.

277   The parcel model simulations are initialized at 90% RH, which is most of the time higher than that

278   measured at ground level. An interpolated radiosonde data product from the BAECC campaign (ARM Data

279   Center, 2014) is used to find temperatures matching 90% RH. Both the temperature measured near ground level

280   (8.4 m above ground level) and the temperature corresponding to 90% RH are shown in Fig. 1c. While these

281   temperatures show similar temporal behavior at times, major differences exist, which can arise from instable

282   temperature profiles as well as sudden changes in air masses that the interpolated data product built from sondes

283   sent three times a day fails to capture. The PNSD and aerosol chemical composition measured near ground level

284   are assumed to be identical to those at 90% humidity, because measurement data at higher altitudes is not

285 available. The volatility distributions retrieved from the FIGAERO-I-CIMS and ACSM data are adjusted to the
286 temperatures obtained from the interpolated radiosonde data product (see Sects 2.3.1 and 2.3.2 for details).

287

288 **2.3 Volatility distributions**

289
290 The total organic (gas + particle phase) volatility distributions are provided as inputs for the ICPM (see Sect.
291 2.1.1). To compare the results from this work to those of Topping et al. (2013), and to assess the changes in co-
292 condensation driven ΔCDNC due to volatility distribution updates from the old particle-phase derived
293 distributions (denoted with CJ; see Sect. 2.3.1) to FIGAERO-I-CIMS-derived distributions (here denoted with F;
294 see Sect. 2.3.2), both approaches are used. The term "volatility distribution shape" refers to the relative proportions
295 of organic mass in each volatility bin, which remain fixed when the partitioning coefficients are iterated (see Eqs.
296 11–13 in Sect. 2.1.1).

297

298 **2.3.1 Volatility distributions based on ACSM measurements (CJ distributions)**

299
300 Previous to the development of the FIGAERO-I-CIMS, organic volatility distributions were probed only through
301 particle phase measurements (e.g., Huffman et al., 2009b), which enabled volatility constraints of relatively low
302 volatility species (Cappa and Jimenez, 2010). More precisely, these early generation OA volatility distributions
303 were obtained from e.g. Aerosol Mass Spectrometer (AMS; Canagaratna et al., 2007) measurements coupled with
304 a thermal denuder (TD; e.g., Huffman et al., 2009a, b). The TD-AMS measurements provide thermograms (mass
305 fractions remaining in the particle phase as a function of TD temperature of ca. 25–250 °C) that could be assigned
306 to individual OA components i.e., low-volatility oxygenated organic aerosol (LV-OOA), semi-volatile
307 oxygenated organic aerosol (SV-OOA), hydrocarbon-like OA (HOA) and biomass burning OA (BBOA). Cappa
308 and Jimenez (2010) then reproduced such thermograms using a kinetic evaporation model (Cappa, 2010) through
309 fitted OA volatility distributions. In this paper, volatility distributions of this kind are referred to as CJ
310 distributions. It is important to keep in mind that the general CJ volatility distribution shape (i.e., the relative
311 proportions of the volatility bins) is assumed to be of the form $C_{i,\,tot} = a_1 + a_2 \exp [a_3(\log_{10} C^* - 3)]$, which was
312 motivated by previous studies on organic aerosol volatility distribution shapes retrieved from chamber
313 experiments (Presto and Donahue, 2006; Robinson et al., 2007), with a_1, a_2 and a_3 as fitting parameters. Later
314 theoretical work on OA volatility distribution retrievals from TD data states, however, that due to uncertainties
315 associated with the enthalpy of vaporization (ΔH_{vap}), mass accommodation coefficients, and volatility distribution
316 shapes, the attained distributions can be reproduced with several combinations of the three (Karnezi et al., 2014).
317   To calculate the CJ distributions for the BAECC OA types, the LV-OOA, SV-OOA and primary organic
318 aerosol (POA; taken as a mix of HOA and BBOA) from the SMEAR II ACSM long-term data set are utilized
319 (Heikkinen et al., 2021). During BAECC, the organic aerosol comprised 63% LV-OOA, 32% SV-OOA and only
320 5% POA on average. Using the time-dependent mass fractions of each OA type, mass-weighted average CJ
321 volatility distributions for each of the model initialization scenarios (97 of them) are calculated. The HOA
322 volatility distribution is used for POA (due to the low abundance of levoglucosan in the ACSM mass spectrum;
323 Heikkinen et al., 2021). Topping et al. (2013) utilized the $\log_{10} C^*$ range of [-6, 3] in their simulations and their
324 example is followed in this work. The CJ volatility distributions have been reported for 298.15 K (Cappa and
325 Jimenez, 2010). As the ICPM simulations are initialized at different temperatures, accounting for the impact these

326   temperature changes had on the volatility distributions is necessary. The relationship between temperature, ΔH_{vap},

327   and C^* is accounted for through an Arrhenius-type Clausius-Clapeyron relation:

$$C^* = C^*(T_{\text{ref}}) \exp\left(\frac{\Delta H_{\text{vap}}}{R} \left(\frac{1}{T_{\text{ref}}} - \frac{1}{T} \right) \right), \quad (16)$$

328   where R is the universal gas constant and T is the ambient temperature in Kelvin (the ICPM initialization

329   temperature), and T_{ref} is 298.15 K. For the relationship between ΔH_{vap} (in J mol^{-1}) and C^* the semi-empirical

330   parameterization under 300 K provided in Epstein et al. (2010) is used:

$$\Delta H_{\text{vap}} = -11 \log_{10} C^*(T_{\text{ref}}) + 129, \quad (17)$$

331   where ΔH_{vap} is the change in heat (enthalpy) of vaporization in kJ mol^{-1}. A lower limit of 20 kJ mol^{-1} is set to the

332   ΔH_{vap}, which is close to the ΔH_{vap} determined for formic acid (NIST Chemistry WebBook, 2022). Eq. (17) would

333   otherwise provide too low, unphysical and even negative values. After the temperature adjustments, the volatility

334   distributions are binned to ranges between $\log_{10} C^* = [-8, 3]$ spaced by one decade in C^* as after adjustments with

335   Eqs. (16–17). The lower limit is reduced by two orders of magnitude, but the upper limit remains as the

336   initialization temperatures did not exceed 300 K. The campaign average CJ volatility distribution is shown with

337   black bars in Fig. 2a. However, each simulation utilizes a unique distribution constructed using the LV-OOA, SV-

338   OOA, and POA time series.

339

340   **2.3.2 Volatility distributions based on FIGAERO-I-CIMS measurements (F distributions)**

341   Organic aerosol volatility distributions from FIGAERO-I-CIMS measurements conducted during BAECC (Mohr

342   et al., 2017, 2019; Schobesberger et al., 2016; Lee et al., 2018, 2020) are also derived. It can be assumed that the

343   FIGAERO-I-CIMS detected most of the OA measured with the ACSM. This is because with the iodide adduct-

344   ionization, FIGAERO-I-CIMS is most sensitive to oxidized organic species, such as organic acids (Lutz et al.,

345   2019), but not sensitive to non-oxidized hydrocarbons (dominating AMS-derived HOA) and as mentioned in Sect.

346   2.3.1. The OA measured with the ACSM comprised on average 95% oxygenated organic aerosol (LV-OOA +

347   SV-OOA), which is generally thought to represent organic acids (Yatavelli et al., 2015). The agreement between

348   the two measurements is supported by the comparison between the daytime FIGAERO-I-CIMS particle phase

349   signal (of identified ions) and the OA mass concentration retrieved from ACSM measurements provided in Fig.

350   S.1. While the quantification of the FIGAERO-I-CIMS measurements remains challenging and therefore a

351   quantitative comparison between the concentrations is uncertain, the high correlation between measurement data

352   (Pearson $R = 0.79$) proves that the instruments generally sample the same aerosol population. Notably, the ICPM

353   simulations obtain OA mass fraction (f_{Org}) only from the ACSM measurements. The volatility distributions are

354   derived from FIGAERO-I-CIMS data using molecular formula parameterizations derived under 300 K in Li et al.

355   (2016):

$$\log_{10} C^*(T_{\text{ref}}) = \left(n_C^0 - n_C \right) b_C - n_O b_O - 2 \frac{n_C n_O}{(n_C + n_O)} b_{CO} - n_N b_N, \quad (18)$$

356   where n_C^0 is a reference carbon number; b_C, b_O, and b_N are the contributions of each carbon, oxygen, and nitrogen

357   atom to the $\log_{10} C^*$, respectively; b_{CO} is a so-called carbon-oxygen non-ideality parameter (Donahue et al., 2011);

358   n_C, n_O, and n_N are the numbers of carbon, oxygen, and nitrogen atoms in the molecular formulae assigned for the

359   FIGAERO-I-CIMS data during high resolution peak fitting of the measured mass spectra. The b-values utilized

360   are listed in Li et al. (2016). In their recent work, Huang et al. (2021) derived volatility distributions from various

361   organic vapor measurements from SMEAR II. They adjusted the Li et al. parameterization for organic nitrates.

362   As shown in Isaacman–VanWertz and Aumont (2021), the utilization of the Li et al. parameterization for OA rich

363   in organic nitrates leads to biased vapor pressure estimates. Organic nitrates are known to form in the boreal air

364   as a result of nitrate radical chemistry, which is pronounced during night, along with daytime oxidation of

365   monoterpenes in the presence of nitric oxide (e.g., Yan et al., 2016; Zhang et al., 2020). To account for these

366   nitrates, Huang et al. (2021) followed the suggestions presented in Daumit et al. (2013) and treated all the nitrate

367   functional groups as hydroxyl (—OH) groups. Given that the focus of this study is on the same measurement site

368   as Huang et al. (2021), their methodology for deriving a volatility distribution from the FIGAERO-I-CIMS is

369   followed here. Once the volatility distributions are constructed using Eq. (18) for 300 K (reference temperature),

370   their adjustments to the parcel model simulation initial temperatures using Eqs. (16–17) are performed.

371   The volatilities are calculated for the 1596 ions identified by the FIGAERO-I-CIMS measurements and

372   afterwards binned with one decadal spacing so that all the extremely low volatility organic compounds (ELVOC)

373   are summed into one bin at $C^* = 10^{-4}$ µg m^{-3}. This is assumed to be appropriate as ELVOCs contain little or no

374   gas phase signals post-initialization (See Sect. 2.1.1). The highest volatilities reached $C^* = 10^7$ µg m^{-3}, which is

375   therefore set as the upper limit of the volatility distribution. Following from this, the volatility span is $\log_{10}C^* =$

376   [-4, 7]. The campaign average volatility distribution is shown in red bars in Fig. 2a. The average CJ distribution

377   exhibits generally higher fractions in the ELVOC region as compared to the F distribution (Fig. 2a). This mostly

378   results from the low or non-existent SVOC and IVOC concentrations in the CJ distribution. The F distributions

379   show a remarkable agreement with the organic volatility distributions from the BEACHON-RoMBAS field

380   campaign conducted at the Manitou Experimental Forest Observatory in the Colorado Rocky Mountains in

381   summer 2011 (Hunter et al., 2017, see Fig. 2a). Hunter et al. (2017) derived a volatility distribution for the total

382   atmospheric reactive carbon (other than CH_4, CO_2 and CO) using six different types of measurements and

383   assuming minimal overlap among the measured species. This volatility distribution is displayed in Fig. 2a after

384   shifting it to the mean ICPM initialization temperature (280 K) using Eqs. (16–17) and subtracting VOC signals

385   from it for comparison.

386   In Figs. 2b and c the partitioning coefficients ξ_q (see Eq. 11) from the ICPM initialization (see Sect. 2.1.1)

387   against the partitioning suggested by the measurements is compared, after accounting for the temperature

388   differences between ground level and ICPM initialization temperatures using Eqs. (16–17). The concentrations in

389   volatility bins with $\log_{10}C^* \leq 1$ agree, suggesting that the majority of the organics in these bins are in the particle

390   phase. Similarly, the agreement in the highest volatility bin ($\log_{10}C^* = 7$) suggests the presence of gas-phase

391   compounds only in both distributions. The estimations of the gas phase vary between $\log_{10}C^*$ 1 and 7, showing a

392   higher gas-phase fraction for the modelled partitioning coefficients. This variability can result from numerous

393   reasons, which apart from uncertainties related to measurements and parametrizations include viscous particle

394   coatings inhibiting equilibration between gas and particle phases, and therefore showing high particle-phase

395   concentrations of high-volatility compounds in the observations. Alternatively, these concentrations can also

396   result from thermal decomposition of lower volatility products during the FIGAERO-I-CIMS heating process

397   (Lopez-Hilfiker et al., 2015) or from the tendency of the Eq. (18) parameterization to underestimate (despite

398   treating the –NO$_3$ groups at –OH groups) the volatility of organic nitrates (Graham et al., 2022), shown to be

399   abundant in the BAECC FIGAERO-I-CIMS data set (Fig. 2e). Understanding these differences is important and

400   requires further analysis.

401   The molecular composition of the gas-phase compounds detected by the I-CIMS during BAECC are
402   analyzed and presented in detail in Lee et al. (2018). In the following, the average composition of each volatility
403   bin during daytime is briefly described. Except for the highest volatility bin, nitrogen-containing species (CHON),
404   which are prominently organic nitrates at SMEAR II (Huang et al., 2021), make up significant mass fractions of
405   each bin in the gas phase (Fig. 2e). Fig. 2f shows the concentration of the gas-phase compounds as a function of
406   the compound carbon and oxygen atom numbers. The figure shows how ELVOCs and LVOCs have the highest
407   numbers of both carbon and oxygen atoms. IVOCs and SVOCs comprise compounds with highly variable carbon
408   skeleton lengths, but the number of oxygen atoms per compound remains low, notably always lowest for IVOCs
409   and VOCs. Formic acid (HCOOH) makes up most of the gas phase signal. It is distributed in the most volatile
410   volatility bin ($C^* = 10^7$ µg m^{-3}). HCOOH is one of the most abundant carboxylic acids in the atmosphere and rain
411   water (e.g., Galloway et al., 1982; Millet et al., 2015 and references therein) and is known to have various sources
412   and precursors (Millet et al., 2015). The I-CIMS measurements discussed here were also performed as part of an
413   eddy covariance flux measurement setup during BAECC (Schobesberger et al., 2016). These flux measurements
414   provided insight into the high HCOOH concentrations possibly due to high emissions from the boreal forest
415   ecosystem. More details from these results can be found in Schobesberger et al. (2016).
416

417   **2.4 ICPM simulation setup**
418   97 daytime scenarios are simulated with ICPM initialization data from BAECC (see Fig. 1a, red crosses). The
419   configuration of ICPM used in this study only considers the adiabatic ascent of an air parcel, without treatment of
420   droplet collision and coalescence, aqueous phase sulfur chemistry or entrainment. Each modelled scenario has
421   log-normal parameters describing a bimodal aerosol size distribution form DMPS measurements followed by
422   Hussein et al. (2005) fitting algorithm. Also, the organic mass fraction from ACSM measurements is given as an
423   input. Organics are present in the simulations as an internal mixture with ammonium sulfate as nitrate is assumed
424   to be organic nitrate (Lee et al., 2018) and the measured sulfate is assumed to be ammonium sulfate, which is
425   generally a good approximation at SMEAR II (Heikkinen et al., 2020). For the simulations performed here, BC
426   is not included given its small (about <5%) contribution to PM$_1$ mass from late spring to summer (Luoma, 2021).
427   The ICPM initialization temperature is taken from interpolated radiosonde data that represents the 90%
428   initialization RH. The atmospheric pressure was set to 980 hPa in all simulation scenarios. The simulations are
429   performed for updraft velocities of 0.1 m s^{-1}, 0.3 m s^{-1}, and 1.0 m s^{-1}, with and without co-condensation for the F
430   distribution. Additional 97 simulations are performed using the 0.3 m s^{-1} updraft with the CJ volatility distribution.
431   Only daytime data (local time between 10:00 and 19:00) are used for the model initializations. Table 1 contains a
432   summary of the simulation input data, which also contains the values used for accommodation coefficient, surface
433   tension, the effective soluble fraction of organics as well as the model time step and number of PNSD size bins.
434   The simulation output, discussed later in the results section of the paper (Sect. 3), is summarized in Table 2. The
435   output data are averaged to a fixed height output grid spaced with a two-meter resolution.
436

437   **2.5 UK Earth System Model (UKESM1) simulations**
438   To evaluate the frequency of times size distributions yielding high ΔCDNC (which is the percent-change in CDNC
439   due to co-condensation) during BAECC would become evident over the boreal biome in an ESM if a
440   parameterization of co-condensation was implemented, the United Kingdom Earth System Model (UKESM1,

441 Sellar et al., 2019; Mulcahy et al., 2020) is utilized. The simulations performed with UKESM1 are configured for

442 Atmospheric Model Intercomparison Project (AMIP) style simulations, where UKESM1 is run in its atmosphere-

443 only configuration with time-evolving sea surface temperature and sea ice as well as prescribed marine biogenic

444 emissions from fully coupled model simulations. In addition to the HadGEM3-GC3.1 core physical dynamical

445 model of the atmosphere, land, ocean and sea ice systems (Ridley et al., 2018; Storkey et al., 2018; Walters et al.,

446 2017), UKESM1 also contains additional component models for atmospheric chemistry and ocean and terrestrial

447 biogeochemistry for carbon and nitrogen cycle representation. A N96L85 horizontal resolution structure (1.875°×

448 1.25° longitude–latitude, which corresponds roughly a horizontal resolution of 135 km) is chosen for the

449 simulations and the vertical space is split to 85 levels (50 levels between 0 and 18 km and 35 levels between 18

450 and 85 km). In this study the model is run in a nudged configuration (horizontal wind nudging (but not

451 temperature) between model levels 12 and 80 with a constant 6-hour relaxation time), for the years 2009–2013

452 inclusively. External forcing and emission datasets are consistent with the Coupled Model Intercomparison Project

453 Phase 6 (CMIP6) implementation as described in Sellar et al. (2020). The simulation setup is same as in the

454 Aerosol Comparisons between Observations and Models (AeroCom) Phase III GCM Trajectory experiment

455 (AeroCom, 2022; Kim et al., 2023, in prep.).

456   The UKESM1 aerosol scheme represents the particle size distributions with five log-normal modes: the

457 nucleation soluble mode, Aitken soluble and insoluble modes, accumulation soluble mode, and coarse soluble

458 mode (Mulcahy et al., 2020). The aerosol microphysical processes of new particle formation (NPF), condensation,

459 coagulation, wet scavenging, dry deposition and cloud processing are handled with GLOMAP (Global Model of

460 Aerosol Processes; Mann et al., 2010; Mulcahy et al., 2020). The UKESM1 NPF mechanism follows the

461 parameterization derived in Vehkamäki et al. (2002) for binary homogeneous nucleation of H_2SO_4 and water.

462 Separate boundary layer NPF is not included in the simulations (Mulcahy et al., 2020). The soluble aerosol size

463 distribution lognormal aerosol modal parameters (nucleation mode, soluble Aitken mode and soluble

464 accumulation mode) and updraft velocities with a 3-hour time resolution at cloud base of stratiform clouds are

465 used. These diagnostics are subsequently masked to include only data in which activated aerosol particles exceeds

466 zero and the temperature exceeds 237.15 K in keeping with criteria used by the droplet activation scheme. The

467 PNSD modal parameters are used to construct aerosol size distributions. In UKESM1 the geometric standard

468 deviations are fixed parameters. The same values are used for consistency for the modes that are accounted for in

469 this work. The geometric standard deviation for UKESM1 Nucleation soluble mode and the Aitken soluble mode

470 is 1.59, and for the accumulation soluble mode it is 1.40. UKESM1 outputs for the Aitken insoluble mode and

471 coarse mode are not used in analysis performed in this study because they do not contribute to CCN in the model

472 representation of cloud droplet activation.

473 **3 Results and discussion**

474 **3.1 Organic condensation: time and volatility dependencies**

475 The first cloud parcel model simulation results (Fig. 3) correspond to initializing the model with data collected on

476 May 11, 2014 at 11:30 EET (East European winter time). This simulation is identified from the full dataset as one

477 that represents a strong cloud response to co-condensation of organics and water. Fig. 3a shows the vertical

478 evolution of total SVOC and IVOC concentrations in the gas phase for the three different updraft scenarios ($w =$

479 0.1, 0.3, or 1 m s^{-1}, respectively). Both SVOC and IVOC concentrations decrease significantly along the adiabatic

ascent in subsaturated conditions below cloud base (CB, RH_{CB} = 100%). "Below CB" is defined as the ascent from RH = 90% upwards as long as RH < 100%. SVOCs and IVOCs are further scavenged inside the cloud in saturated conditions. This result is in line with Bardakov et al. (2020), who modelled complete gas removal of volatility bins up to roughly $\log_{10} C^*$ = 9 within convective clouds.

When considering all 97 simulations, the net mass fractions of organics condensed below CB are on average 91, 72 and 35% for the 0.1, 0.3 and 1.0 m s^{-1} updraft, respectively, which in absolute concentrations means additions of 1.8, 1.4, and 0.7 µg m^{-3} to the aerosol particle soluble mass (Table 2). The yielded mass concentrations are in the same order of magnitude of the PM$_1$ mass concentrations measured during BAECC (interquartile range, IQR: 0.95, 1.95, and 3.22 µg m^{-3} from ACSM data), which means that such organic condensation along the adiabatic ascents simulated here would yield roughly a doubling of the soluble mass due to SVOC and IVOC condensation below CB. These numbers should, however, be assessed with caution as an ideal liquid phase, as well as partitioning being determined by mole fractions of water-soluble organics are assumed in this work (Sect. 2.1.1).

Topping et al. (2013) looked into the assumption of ideality in their supplementary material. They found it to enhance the amount of modelled organic condensate as compared to a non-ideal case. However, their simulations exploring non-ideality with organic activity coefficients predicted with the UNIFAC method (UNIQUAC Functional-group Activity Coefficients; Fredenslund et al., 1975) or solubilities still led to significant amounts of condensed organic mass. The impact of the ideality assumption was shown to be most significant in their highest volatility bin (C^* = 1000 µg m^{-3}). Activity coefficients and solubilities of organics should in the future be better constrained to assess the impact on volatility bins of $\log_{10} C^* > 3$, which was not explored in Topping et al. (2013). As discussed in the Topping et al. (2013) supplementary information, it is likely that solubility decreases towards the higher volatility bins.

Further investigation on how efficiently different volatility bins condensed along the adiabatic ascents across all the 97 simulation scenarios repeated with the three fixed updraft velocities is also performed (Fig. 4). In the 0.1 m s^{-1} updraft scenario, almost all organic vapor condenses up to $\log_{10} C^*$ = 5 and the condensation capability of the highest volatility bin ($\log_{10} C^*$ = 7) shows the highest variability (30–100% condensed below CB; Fig. 4a). The same features can be observed with the 0.3 m s^{-1} and 1.0 m s^{-1} updraft simulations, although the fraction of organic vapor condensed per volatility bin is reduced (in the w = 1 m s^{-1} scenarios only ca. 40% of the vapor condenses below CB (Figs. 4b–c). The results from these simulations reveal that there is enough time under slow adiabatic ascents for most of the organic vapor to condense.

Figures 4d–f show the simulated organic condensate concentrations for each volatility bin. While the fraction condensed for the highest volatility bin is lowest (Figs. 4a–c), the absolute concentrations are amongst the highest due to the high availability of organic vapor in the highest volatility bin (mostly HCOOH; Sect. 2.3.2). The condensation efficiency of the highest volatility bin shows a high ICPM initialization temperature dependence. If the model initialization takes place at 270 K, up to 100% of the organic vapor in the bin condenses, while if the ascent starts at 290 K, only 40% of the mass concentration is transferred to the condensed phase below CB (Figs. 4g–i). A closer look into Figs. 4g–i reveals that under similar temperature, the condensation of the $\log_{10} C^*$ = 7 bin is most efficient in the presence of a high concentration of accumulation mode particles. This suggests that these organic vapors are likely to condense onto larger particles, which are susceptible to be activated into cloud droplets regardless of co-condensation. Similar correlations are observed to a lesser extent with the

520    $\log_{10}C^* = 6$ volatility bin (not shown). In this work, the information of the size ranges of particles which the high-

521   volatility IVOCs condense onto is lacking. Therefore, more systematic studies should be conducted to better

522   understand whether the condensation of the high-volatility IVOCs onto ultrafine particles is sufficient enough to

523   lead to droplet activation.

524   As the results from Figure 4 underline the time-dependence of co-condensation, it is worth remembering

525   that the ICPM initialization RH is set to 90% (see Sect. 2.4). If the initial RH was set to a lower value, more time

526   would be available for co-condensation before reaching CB, and if the initial RH was set to a higher value, less

527   time would be available. While the decision of maintaining a fixed initial RH for the different simulations is

528   proven useful for this study as it eases the data interpretation process, it should be acknowledged that the initial

529   RH could be better constrained in future simulations.

530

3.2 Impact of updraft velocity on the sensitivity of cloud microphysics to organic vapor condensation

532   As explained previously in Topping et al. (2013), the CDNC enhancements associated with co-condensation arise

533   from the enhancement in organic solute concentration, which decreases the critical supersaturation (s^*) needed for

534   a given particle to activate. The s^* reductions from 0.15% to 0.10% for the May 11, 2014 at 11:30 EET case are

535   shown in Fig. 3b, and correspond to a dry radius of 71.9 nm (i.e., the smallest activated dry radius when co-

536   condensation is disabled, r^*_{noCC}, and $w = 0.1$ m s^{-1}; Table 2). Fig. S.2 shows the development of the wet particle

537   size as a function of altitude in the ICPM simulation summarized in Fig. 3. It clearly demonstrates the differences

538   introduced by co-condensation through the activation of new size bins (4 size bins in total when $w = 0.1$ m s^{-1})

539   that remain as interstitial aerosol particles in the simulations, where co-condensation is turned off. The enhanced

540   growth of more particles due to co-condensation enhances the water vapor condensation sink, which leads to a

541   reduction in the achieved maximum ambient supersaturations (s_{max}; see Fig. 3c for the May 11 case and Table 2

542   summarizing all the 97 simulations). As the updraft is the same in simulations performed with and without co-

543   condensation, the condensation sink dictates the changes in s_{max} (Eq. 3). A reduced s_{max} would typically lower the

544   number of aerosol particles activating into cloud droplets, but here the suppressions in s^* are greater than the

545   reductions in s_{max}, which therefore leads to an enhanced CDNC (see Fig. 3b–c for the May 11 case). This can be

546   interpreted as a competition effect between the s_{max} and s^* reductions, respectively, which the s^* reduction wins.

547   When examining the 0.1 m s^{-1} updraft case in the May 11th simulation shown in Fig. 3, the s_{max} is reduced 12.5%

548   (from 0.16% to 0.14%), which is less significant than the s^* reduction of about 33% (from 0.15% to 0.10%; Fig.

549   3b). This leads to a 22% enhancement in CDNC (Fig. 3d) as r^* reduces from 72 nm to 66 nm ($\Delta r^* \approx 6$ nm). Fig.

550   3e finally shows the droplet spectrum for the May 11 case, which highlights the consistent shift of droplet sizes

551   to smaller diameters due to organic co-condensation (see also Fig. S.2, which displays the same May 11th

552   simulation with $w = 0.1$ m s^{-1}).

553   The modelled BAECC campaign median CDNC values (over the 97 simulations) without co-

554   condensation are on average 161, 300 and 530 cm^{-3} in modeling scenarios utilizing 0.1 m s^{-1}, 0.3 m s^{-1}, and 1.0 m

555   s^{-1} updrafts, respectively (Table 2). CDNC is shown to correlate well with the accumulation mode number

556   concentration (N_2), and at times with the Aitken mode number concentration (N_1) if the Aitken mode particles are

557   large enough in size and accompanied with strong enough updrafts and a low N_2 (Fig. S.3). The reductions in the

558   smallest activated critical radii due to co-condensation are on average 8.2, 6.6, and 5.9 nm for the modeling

559   scenarios utilizing 0.1 m s^{-1}, 0.3 m s^{-1}, and 1.0 m s^{-1} updrafts, respectively, and the corresponding median ΔCDNC

560 are 16.8, 23.3 and 20.6%, respectively (Table 2 and Fig. 5a). The swarm plot on Fig. 5a shows that ΔCDNC and
561 CDNC do not correlate i.e., high susceptibility is in this case not predicted specifically for low CDNC.

562 On average during the BAECC simulation period (97 simulations), the highest ΔCDNC are found when
563 initializing the model with a 0.3 m s^{-1} updraft velocity (also visible in Fig. 3d for the May 11 case) followed by
564 ΔCDNC predictions for the 1 m s^{-1} case. In the latter, high supersaturations are achieved leading to the formation
565 of many cloud droplets, yet the effects of co-condensation remained less pronounced as the high ascent speed
566 poses kinetic limitations for organic condensation (see Sect. 3.1 and Fig. 4). Despite the highest organic uptake in
567 the 0.1 m s^{-1} updraft simulations (Fig. 4a, d), the ΔCDNC remains the lowest. This can be explained by the low
568 s_{max}, which remains insufficient for the activation of small particles and kept the smallest activated dry diameter
569 on average at 63.7 nm (Table 2). As the Aitken mode possesses most particles in terms of number (Table 1), the
570 few nm reductions in r^* affect ΔCDNC the most when taking place at the steep slopes between the Aitken and
571 accumulation mode, which does not happen in the simulations performed with 0.1 m s^{-1} updraft.

572 An additional set of simulations using the CJ volatility distribution with the 0.3 m s^{-1} updraft velocity are
573 performed to assess the comparability of our simulations to Topping et al. (2013) and to evaluate the impact of
574 the volatility distribution upgrade from CJ to F. Results from these simulations are summarized in Table 2, but
575 also visualized in black in Figs. 3 and 5a. The ΔCDNC predicted in the simulations using CJ volatility distributions
576 are lower (ΔCDNC = 12.4%) than those predicted using the F distribution, but fall within the variability reported
577 in Topping et al. (2013; ΔCDNC of ~5–55%). The difference between the simulations performed with CJ and F
578 volatility distributions, respectively, can be explained by the lower organic vapor concentration in the CJ
579 distribution at model initialization, leading to a lower amount of soluble mass at CB (Table 2; Fig. S.4). This result
580 highlights that significant quantities of co-condensable organic vapors are distributed in the higher volatility bins
581 and these concentrations should not be neglected in further co-condensation studies.

582

583 **3.3 Impact of initial aerosol size distribution and organic vapor concentration on the sensitivity of CDNC**
584 **to organic vapor condensation**
585
586 The importance of Aitken mode in ΔCDNC associated with turning co-condensation on in ICPM is exemplified
587 in Fig. 5b for the 0.3 m s^{-1} updraft simulations. In this figure, the initial dry PNSD are averaged from the
588 simulations with the highest 50% and lowest 50% modelled ΔCDNC, respectively. The PNSD corresponding to
589 the highest 50% of the modelled ΔCDNC has a very minor accumulation mode and a large Aitken mode (with
590 respect to the mode total number concentrations i.e., N_2 and N_1, respectively). It is therefore named as PNSD$_{NUM}$,
591 where NUM refers to a strong nascent ultrafine mode characteristic of the shown size distribution. The PNSD
592 corresponding to the lowest 50% of the modelled ΔCDNC is strongly bimodal, where the Aitken and accumulation
593 modes are almost equal in terms of N. Moreover, the two modes are separated by a clear Hoppel minimum (Hoppel
594 and Frick, 1990). Hoppel minimum is characteristic for particulate matter, which has undergone cloud processing.
595 This result underlines that environments rich in particles from a local source would be more susceptible to high
596 ΔCDNC due to co-condensation while regions with aged and cloud processed size distributions are affected less
597 (ΔCDNC<20% in our simulations; Fig. 5a).

598 Interestingly, a nascent ultrafine aerosol particle mode (NUM) was found to be important when looking
599 into suitable conditions for large increase in CDNC caused by surface active organics (Lowe et al., 2019;
600 Ovadnevaite et al., 2017). Lowe et al. (2019) utilized the same CPM as used in this study (notably without co-

601   condensation), but enabled a fraction of the particulate organics to form a thin, max. 0.2 nm thick film around the

602   particle. The film was characterized by a surface tension of 40 mN m^{-1} as opposed to the surface tension of pure

603   water (72.8 mN m^{-1}). The idea of this compressed film (CF) approach was to simulate the surface tension

604   reductions caused by organic species leading to the activation of smaller particles to cloud droplets at the coastal

605   Mace Head site (Ovadnevaite et al., 2017). Through sensitivity studies, Lowe et al. (2019) found that the largest

606   percent change in CDNC due to surface active organics (>10%) took place in Mace Head when $N_2 < aN_1^b + c$ ($a =$

607   602, $b = 0.0884$, $c = -766$). The increase in CDNC in the Lowe et al. (2019) study was also attributed to the

608   reduction in s_c when comparing against simulations where the surface tension was that of water. Moreover, the

609   same competition effect between s_{max} and s_c reductions – as described here in Sect. 3.2 – was demonstrated in

610   their study, but just triggered by different chemical parameters. The sensitivity of the CDNC enhancements to

611   PNSD$_{NUM}$ in this study as well as in Lowe et al. (2019) demonstrates that the activation of fresh and non-cloud-

612   processed aerosol particles is susceptible to small reductions in s_c that can be triggered e.g., by organic surfactants

613   or co-condensation. Importantly, potential surface activity also affects the CCN activation behavior of

614   atmospheric organics (Ruehl et al., 2012, 2016; Lowe et al., 2019), correlating with volatility and solubility. The

615   combined effect of all these three properties needs to be thoroughly investigated, because of the potential of the

616   organic film to suppress the solute effect (Sorjamaa et al., 2004) and thereby co-condensation and its effects on

617   ΔCDNC.

618   In conjunction with the ΔCDNC susceptibility to PNSD$_{NUM}$, this study most critically highlights the

619   importance of incorporating multimodal, and representative size distributions in process modeling studies

620   examining the cloud response to surface active organics, or co-condensation. Topping et al. (2013), for example,

621   used monomodal distributions (with varying log-normal parameters) in their study, which could lead to

622   overestimation of ΔCDNC as size distributions with Hoppel minima are not explored. Multimodal distributions

623   were used later by Crooks et al. (2018), but further explanation of the cloud response of the update remained

624   lacking. In summary, our results suggest that in clean environments with a local source of ultrafine particles, such

625   as the boreal forest or marine environments, organic species in the presence of a NUM-featured PNSD can have

626   significant impact on cloud properties either via co-condensation or through surface tension reductions.

627   Subsequently, a dry PNSD-based criteria for identifying regimes (conditions) in which co-condensation

628   has the highest impact on CDNC are defined. It is found that restricting the ratio between the accumulation and

629   Aitken mode geometric mean diameters in the initial dry PNSD to below six (i.e., $D_2/D_1 < 6$) and the Aitken mode

630   number concentration to exceed 1000 cm^{-3} (i.e., $N_1 > 1000$ cm^{-3}) would yield ΔCDNC >20% in our simulations.

631   By using the diameter ratio criterion, size distributions without a distinguishable Hoppel minimum are selected,

632   which is characteristic in the simulations yielding the highest ΔCDNC (Fig. 5b) and the high N_1 ensures a high

633   concentration of aerosol particles potentially activating into cloud droplets. Fig. 5d shows the ΔCDNC as a

634   function of D_2/D_1, N_1 and the Pearson correlation coefficient with PNSD$_{NUM}$ (0.3 m s^{-1} updraft case). The

635   simulations with the initial dry PNSD fulfilling the criteria are highlighted with white crosses. Most of the high

636   ΔCDNC are well captured, and at those times the correlation with the PNSD$_{NUM}$ is high (Pearson $R > 0.7$). The

637   simulations fulfilling the dry PNSD-based criteria are marked also in Fig. 5c showing that most of the high

638   ΔCDNC are captured, which again highlights the critical role of the aerosol size distribution representation in

639   capturing the co-condensation driven ΔCDNC.

640   In addition to the $PNSD_{NUM}$ features, also the initial organic vapor concentration (C_g^{INIT}) influences the

641   modeled ΔCDNC. This relationship is depicted in Fig. 5c using the ICPM simulations corresponding to 0.3 m s^{-1}

642   updrafts. The y–axis represents the modeled ΔCDNC and the x-axis the organic vapor concentration distributed

643   in $\log_{10}C^*$ bins within [-4, 4] (denoted as $C_{g,-4:4}^{INIT}$) i.e., in bins that do not show high dependency on N_2 or initial

644   temperature (see Sect. 3.2 for details). The relationship is not straightforward, but linear increases in ΔCDNC as

645   a function of $C_{g,-4:4}^{INIT}$ can be seen under constant, yet sufficiently high s_{max} (here >0.2%). Under the modelled

646   scenarios where s_{max}>0.2%, the $C_{g,-4:4}^{INIT}$ remains low, mostly below 2 μg m^{-3}, and the highest enhancements are

647   achieved when $C_{g,-4:4}^{INIT}$ is ≲1 μg m^{-3} because the soluble organic mass is distributed to more particles. The markers

648   in Fig. 5c are color-coded by the initial PNSD surface area, which under a constant updraft anticorrelates with

649   s_{max} (see Eq. 3). ΔCDNC shows high sensitivity to $C_{g,-4:4}^{INIT}$ when the dry PNSD surface area stays below a 100 μm^2

650   cm^{-3} threshold. Based on this analysis, it can be concluded that in the presence of a NUM-featured PNSD enabling

651   the formation of high supersaturations (the dry PNSD surface area stays below 100 μm^2 cm^{-3}), an adiabatic ascent

652   with an updraft of 0.1 or 0.3 m s^{-1} can yield ΔCDNC of >40% if 1 μg m^{-3} of co-condensable organic vapor is

653   present in the rising air. This is a likely occurrence in the spring and summertime boreal forest (Huang et al.,

654   2021). The simulations performed with the highest updraft velocity (w = 1.0 m s^{-1}) yield lower ΔCDNC under

655   these clean conditions (ΔCDNC does not exceed 40%) even though the simulated s_{max} increase as opposed to the

656   results obtained with lower updrafts (e.g. Table 2), because of the kinetic limitations hindering co-condensation

657   (see Sect. 3.1).

658

659   **3.4 Expected seasonality in the impact of co-condensation on CDNC at SMEAR II**

660   In the following, the seasonality of the dry PNSD surface area at SMEAR II (6-year-long time series, 2012–2017)

661   is investigated to estimate how often it stays below the previously mentioned threshold of 100 μm^2 cm^{-3} i.e., times

662   when only 1 μg m^{-3} of co-condensable organic vapor present in the rising air could yield significant ΔCDNC. This

663   is followed by an investigation of the frequency of the PNSD criteria (D_2/D_1<6 and N_1>1000 cm^{-3}) fulfillments in

664   the long-term size distribution measurements at SMEAR II.

665   Fig. 6a shows the seasonality of the dry surface area at SMEAR II. During daytime (9–19 EET) the

666   surface area stays below the previously mentioned threshold 86% of the time during the 2012–2017 measurement

667   period (Fig. S.5), which suggests that under 0.3 m s^{-1} updraft velocities, generation of s_{max}>0.2% at this site is

668   likely. During summer months, the likelihood of surpassing the dry PNSD surface area threshold of 100 μm^2 cm^{-3}

669   increases to 22% from 10% (Fig. S.5) due to biogenic SOA formation (Tunved et al., 2006), which grows the

670   accumulation mode in the PNSD. Biogenic SOA formation depends on the SOA precursor i.e., BVOC emissions

671   and concentrations. Monoterpene concentrations are highest at SMEAR II in summer (Kontkanen et al., 2016;

672   Hakola et al., 2012) as their emissions are strongly temperature-driven (Guenther et al., 1993). The organic vapor

673   concentration available for co-condensation is therefore also highest in summer, but due to the enhanced surface

674   area, the soluble organic mass is distributed to more particles dampening the cloud response to co-condensation.

675   However, the monoterpene emission period is longer than just summer, and elevated monoterpene concentrations

676   can be observed throughout the thermal growing season (when the daily average temperature is above 5°C;

677   Kontkanen et al., 2016; Hakola et al., 2012). Therefore, monoterpene emissions take place also at times when the

678   dry PNSD surface area stays below the 100 μm^2 cm^{-3} threshold.

679   Fig. 6b shows the dry PNSD surface area derived from the long-term PNSD measurements at SMEAR

680   II as a function of temperature. When the ambient temperature exceeds 5°C, the dry PNSD surface area starts to

681   increase with increasing temperature. The dry PNSD surface areas and ambient temperatures (from 8.4 m height;

682   Fig. 1c) from the BAECC simulation period are also shown to highlight the fact that the BAECC sample represents

683   well the long-term statistics of the thermal growing season, providing confidence in the representativity of the

684   BAECC sampling period for this boreal environment. The BAECC samples are color-coded by the modelled

685   ΔCDNC. The highest ΔCDNC (i.e., ΔCDNC > 40%) are modeled when the dry PNSD surface areas are below

686   the 100 μm^2 cm^{-3} threshold. Importantly, most of these model scenarios yielding ΔCDNC > 40% coincide with

687   ambient temperatures between 5 and 8°C i.e., at times when the monoterpene concentrations are not at their

688   highest yet sufficient concentrations of organic vapor are still present to cause a large cloud response. It can

689   thereby be concluded that the highest ΔCDNC due to co-condensation can be expected in thermal Spring and Fall.

690   However, due to the seasonality in hygroscopicity and the slightly higher κ in spring and autumn (as opposed to

691   summer; Fig. 6a) the likelihoods of obtaining s_{max} exceeding 0.2% to yield significant ΔCDNC can be somewhat

692   buffered due to hygroscopic growth.

693   Next, the frequency to which the PNSD criteria (D_2/D_1<6 and N_1>1000 cm^{-3}) are fulfilled in the long-

694   term size distribution measurements is examined. For this purpose, the same 6-year PNSD data set collected at

695   SMEAR II fitted with two log-normal size distributions (Hussein et al., 2005) is utilized. The percentage of times

696   the criteria are met is shown in Fig. 7a. The highest frequencies (30–40% of the time) are observed in April, May

697   and September, which correlates with the new particle formation (NPF) frequency at the site (Nieminen et al.,

698   2014; Dada et al., 2017). The monthly median size distributions fulfilling the criteria are shown in Fig. 7c. They

699   all clearly exhibit the lack of a Hoppel minimum, similarly to PNSD$_{NUM}$, and suggest a potentially high impact of

700   newly formed particles on cloud properties through co-condensation. The results again clearly emphasize the need

701   of accurate representation of aerosol size distributions and lifecycle in models (such as other CPMs or global

702   circulation models, GCMs) to account for the impacts of co-condensation and the strong seasonality to be expected

703   in the magnitudes in ΔCDNC.

704

705 3.5 Expected spatiotemporal variability in the impact of co-condensation on CDNC over the boreal biome
706

707   In this section the SMEAR II results are compared against a 5-year UKESM1 simulation (see Sect. 2.5; analysis

708   restricted to the boreal biome). While the SMEAR II PNSD data are retrieved at ground level, utilization of the

709   UKESM1 modal parameters (only soluble modes considered) from CB is chosen, because these PNSD log-normal

710   parameters would actually meet the cloud droplet activation scheme in the model. The monthly averages of the

711   percentage of times the criteria (D_2/D_1<6 and N_1>1000 cm^{-3}) are fulfilled in the boreal grids are shown in Fig. 7b.

712   Here, the Aitken mode geometric mean diameter and total number concentration (D_1, N_1) and accumulation mode

713   geometric mean diameter (D_2) are obtained from the soluble Aitken and accumulation modal parameters (see Sect.

714   2.5 for more details regarding the UKESM1 modes). The frequencies, which remain roughly well below 6%, are

715   in general much lower than observed at SMEAR II. This can be explained by the lack of the boundary layer NPF

716   process in the UKESM1 simulations (Sect 2.5). Therefore, the UKESM1 results can be taken as the lower estimate.

717   Fig. 7d displays the monthly median PNSD in the boreal grid cells fulfilling the criteria (D_2/D_1<6 and N_1>1000

718   cm^{-3}), which are constructed from the soluble Nucleation, soluble Aitken and soluble accumulation mode modal

719   parameters from the UKESM1 simulations when the criteria are fulfilled (criteria only uses soluble Aitken and

soluble accumulation modes). The size distributions calculated using these UKESM1 modal parameters are in general less similar to the PNSD$_{NUM}$ than the monthly median SMEAR II size distributions are (Fig. 7c), because they have more distinguished multimodal shapes. However, they still feature a minor accumulation mode in the presence of a large Aitken mode (with respect to N).

The UKESM1 results suggest strong spatiotemporal variability in the co-condensation driven ΔCDNC should be expected if this process were to be represented in GCMs. Consistently with the SMEAR II observations (Fig. 7a), spring months stand out as the times when the criteria are most likely to be met, but the other peak in the frequency, expected in September at SMEAR II, cannot be seen. Another interesting feature is the large spatial variability in the frequency. In March and April, a very evident hotspot can be seen in the southern parts of the boreal forest, more precisely in the north of Kazakhstan. When the whole northern hemisphere is displayed, it is clear that the hot spot region extends over Europe during Spring (Fig. S.6) when the conditions favor the formation, growth and survival of small particles (Kerminen et al., 2018) as shown in Fig. S7 in terms of nucleation mode number concentration. The result therefore suggests high co-condensation potential in areas rich in ultrafine particles. The cloud response of co-condensation in an extended domain covering most of Eurasia could be an interesting follow-up study. However, such a study should incorporate also the condensation of nitric acid and ammonia, the concentrations of which are presumably abundant in the regions, where the co-condensation PNSD criteria are met (Kakavas et al., 2022). As this "Kazakhstan hotspot" is connected to aerosol phenomenology outside the boreal biome, the analysis is not continued further. Another evident springtime hot spot is located in North America, near the Rocky Mountains, but the updraft velocities at the area are not within the desired range ([0.2, 0.5] m s^{-1}) to yield significant cloud response from co-condensation (Fig. 7b).

Aside from these hotspots, it is notable that the overall background of the frequency of the times the criteria are met in the latitude range of [0, 75] °E increases from <2% to 2–6% when moving from March to April. This background stays elevated until June. Smaller hotspots within this area are visible and they correspond to regions known with high sulfur dioxide (SO$_2$) emissions, such as the Kola peninsula. The Kola peninsula SO$_2$ emissions have shown to trigger NPF events measured at SMEAR I in Finnish Eastern Lapland (e.g., Kyrö et al., 2014). An interesting next step would be to see how Fig. 7b changes with UKESM1 simulations incorporating boundary layer NPF and whether the percentage of times the criteria are met increases to values comparable with the SMEAR II observations and whether the frequency becomes larger also in Fall. Another interesting observation to be made from Fig. 7b is that no significant impact of co-condensation would be expected in UKESM1 in most of Siberia (East and Northeastern Siberia), which can be explained by the lack of nucleation mode particles in the UKESM1 simulations over the region (Fig. S.7).

4 Conclusions

This study focuses on the role of the co-condensation of organic vapor and water on warm cloud microphysics in a boreal forest environment. Co-condensation has been proposed as a potentially significant process contributing to the feedbacks between VOC emissions, SOA loadings, cloud formation and climate. Boreal forests account for about a third of the Earth's forested area and are potentially significant sources of such co-condensing species.

First, ICPM model is used to perform simulations for the BAECC measurement campaign which took place at the SMEAR II station in Southern Finland during 2014 (Petäjä et al., 2016). The measurement setup during BAECC was very advanced, enabling the initialization of ICPM with state-of-the art data describing the

ambient aerosol physical and chemical properties. The measurements conducted with the FIGAERO-I-CIMS (e.g., Mohr et al., 2017) are of high importance for this study due to the simultaneous measurements of organic particle and vapor species. These data enable the incorporation of organic vapors from a broad volatility range into the ICPM simulations. The previous modeling work on this topic used volatility distributions based on particle-phase measurements only, resulting in overall lower volatility and contributions of semi- and intermediate volatility organic vapor.

The results from the ICPM simulations reveal that a competition effect exists between the reductions in maximum supersaturations and critical supersaturations needed for aerosol particle activation into cloud droplets. The reductions in critical supersaturations are greater than the reductions in maximum supersaturation, which results in the simulated CDNC enhancements (simulations with co-condensation are compared against simulations without it under same meteorological conditions). The CDNC enhancements are of the order of 20% under realistic updraft velocities (0.1, 0.3, and 1 m s^{-1}) and correspond to reductions of 12–16 nm in the smallest activated dry diameters (144 to 126 nm, 102 to 88.6 nm, 72 to 61 nm for the 0.1, 0.3, and 1 m s^{-1} updraft scenarios, respectively). The activation of smaller particles into cloud droplets results, as expected, in the formation of more numerous smaller cloud droplets. The critical supersaturation suppressions result from the additions of soluble organic mass below cloud base along the simulated air parcels' adiabatic ascents while the reductions in maximum supersaturation are caused by the increasing condensation sink provided by more cloud droplets (the source of supersaturation is fixed as the meteorological conditions between simulations with and without co-condensation are kept constant).

The predicted CDNC enhancements are highest for the 0.3 m s^{-1} updraft velocities and depend on several, at least partly, interlinked parameters (see also Lowe et al., 2019). One parameter affecting the modelled CDNC is the availability of the co-condensable organic vapors, which in turn depend on the updraft velocities and the features of the organic volatility distribution. Most organic vapor condenses under the slowest adiabatic ascents and least in the highest due to kinetics. The organic volatility bins spanning from ELVOCs to the lower-volatility IVOCs condense in a similar, updraft-dependent, degree prior reaching the cloud base. Organic vapors of higher volatility involving species such as formic acid condense less efficiently and their condensation is sensitive to the model initialization temperature and the presence of large particles, which are likely to activate regardless of co-condensation. Therefore, small enhancements in particularly SVOC and lower-volatility IVOC concentrations lead to significant enhancements in CDNC, while increases in the most volatile IVOCs and formic acid do not affect CDNC much.

The simulations performed with 0.3 m s^{-1} updrafts are repeated using volatility distributions from previous co-condensation studies (Cappa and Jimenez, 2010; Topping et al., 2013; Crooks et al., 2018). By doing so, the BAECC campaign median CDNC enhancement decreased from 23.3 to 12.4%. This result is explained by the lower SVOC and IVOC concentrations in previous studies, highlighting the added value of capturing these higher volatility bins within the VBS representations of atmospheric organic species. On the other hand, adding information on the LVOC and ELVOC range do not significantly influence the CDCN enhancements due to co-condensation.

The sensitivity of the modelled ΔCDNC to organic vapor concentrations is strongest when high maximum supersaturations (s_{max}>0.2% for the 0.3 m s^{-1} updraft scenarios) are reached. Such conditions are achieved when the dry PNSD surface area (a proxy for the condensation sink) remains below 100 μm^2 cm^{-3}. Under

800 those conditions, CDNC enhancements exceeding 40% are predicted for conditions in which roughly 1 µg m^{-3} of

801 co-condensable organic vapor is present.

802 Besides the updraft velocities and the availability of co-condensable vapors, the CDNC enhancements

803 depend critically on the size distribution of the initial aerosol population. Highest CDNC enhancements are

804 generally achieved when the model is initialized with a relatively weak accumulation mode combined with a large

805 nascent ultrafine particle mode with a geometric mean diameter of ca. 40 nm, with no visible Hoppel minimum

806 present in the distribution. Such conditions are observed most frequently in Spring and September (about 30–40%

807 of the time in years 2012–2017), when new particle formation events take place at SMEAR II.

808 Further on, UKESM1 simulations (years 2009–2013) are utilized to investigate the potential impact of

809 including the process of co-condensation on droplet formation in this model over the whole boreal biome using

810 the criteria developed from the SMEAR II case to identify most susceptible PNSD conditions. Aside from two

811 hotspots (one near the Rocky Mountains in North America, one over northern Kazakhstan, which are not analyzed

812 further), the presence of suitable PNSD is most frequent over Fennoscandia and western parts of Siberia in spring,

813 yet the frequencies at which those PNSD are modelled remained much lower than those obtained from the long-

814 term SMEAR II PNSD measurements (2–6% in UKESM1). It is likely that the incorporation of boundary layer

815 NPF in UKESM1 will increase this frequency. Perhaps surprisingly, suitable PNSD are never modeled over most

816 of Siberia, suggesting that for the model configuration of UKESM1 used in this study, the process of co-

817 condensation would not be expected to have an influence on droplet formation in this area. This is due to the low

818 concentration of ultrafine particle particles modeled in the area.

819 In summary, these results highlight the potential significance of co-condensation in pristine boreal

820 environments with a nascent ultrafine particle mode present. Such conditions are met over Fennoscandia and

821 Western parts of Siberia in Spring and to a lesser extent in the Fall, when NPF takes place. For future modelling

822 purposes, it is vital to stress the importance of the accurate representation of PNSD for capturing the role of co-

823 condensation of organics on CDNC enhancements. Because the modelled CDNC enhancements are so significant,

824 further research focus especially regarding observations of the co-condensation should be targeted in the future to

825 motivate future assessments of co-condensation-driven radiative forcing. Perhaps this work inspires aircraft

826 measurements (of the relevant parameters discussed in this paper) to take place over the Fennoscandia in the future

827 to finally narrow down the importance of co-condensation.

828

829

Data availability

831 The ICPM input and outputs for reproducing the figures will be available on the Bolin Centre database.

Competing interests

833 The authors have the following competing interests: Some authors are members of the editorial board of
834 Atmospheric Chemistry and Physics. The peer-review process will be guided by an independent editor. On or
835 more authors have received funding from European Union's Horizon 2020 research and innovation programme,
836 European Research Council, Knut and Alice Wallenberg foundation, Academy of Finland and US Department of
837 Energy, and/or support from ACTRIS Translational Access and ACTRIS-HY. The authors have no other
838 competing interests to declare.

Author contributions

840 LH, IR, DGP and CM conceptualized the idea of the study. LH prepared the model input data performed the
841 simulations, analyzed the simulation output, made the figures and wrote the manuscript with contributions from
842 the coauthors. TP designed and led the BAECC campaign. CM performed the FIGAERO-I-CIMS measurements,
843 WH processed and delivered the FIGAERO-I-CIMS data and gave input on the volatility distribution calculation.
844 RR assisted with the radiosonde data and provided the hygroscopicity seasonal cycle data. ET and DGP performed
845 the UKESM1 simulations and DGP designed and processed the data for analysis input parameters to droplet
846 activation parameterization. SB visualized the UKESM1 data and gave input on the data interpretation. LH wrote
847 the paper with input from all co-authors.

Acknowledgements

849 We gratefully acknowledge Samuel Lowe for developing the unified framework for organics onto the ICPM
850 (Lowe, 2020), the useful discussions, code and support. We acknowledge Ellie Duncan for useful discussions and
851 support regarding the UKESM data. We acknowledge Pasi Aalto and SMEAR II staff for their efforts during the
852 BAECC campaign and Dmitri Moisseev for useful discussions regarding updraft velocities. We thank Federico
853 Bianchi for useful discussion regarding NPF in the Northern Hemisphere. We acknowledge the Atmospheric
854 Radiation Measurement (ARM) Program for their inputs during BAECC, the interpolated radiosonde data were
855 obtained from the ARM Program sponsored by the U.S. Department of Energy, Office of Science, Office of
856 Biological and Environmental Research, Climate and Environmental Sciences Division. We acknowledge use of
857 the Monsoon2 system, a collaborative facility supplied under the Joint Weather and Climate Research Programme,
858 a strategic partnership between the Met Office and the Natural Environment Research Council. We also thank all
859 the people responsible for the development of UKESM1. DGP would like to extend a personal thanks to Dr
860 Alistair Sellar, who provided support for the configuration of the UKESM1 simulations performed as part of the
861 AeroCom GCM Trajectory experiment on which these simulations are based.

Funding

863 Financial support from the European Union's Horizon 2020 research and innovation programme (project FORCeS
864 under grant agreement No 821205, project FOCI under grant agreement No101056783, project CRiceS under
865 grant agreement No 101003826), European Research Council (Consolidator grant INTEGRATE No 865799,
866 starting grant CHAPAs No 850614), and Knut and Alice Wallenberg foundation (Wallenberg Academy
867 Fellowship projects AtmoRemove No 2015.0162 and CLOUDFORM No 2017.0165) , Academy of Finland via a
868 Flagship programme for Atmospheric and Climate Competence Center (ACCC, No 337549) and projects No
869 353386, 334792, 340791, 325681 are gratefully acknowledged. The BAECC campaign was supported by US
870 Department of Energy (Petäjä, No DE-SC0010711) and additional measurements were supported via ACTRIS
871 Transnational Access. University of Helsinki is acknowledged for supporting the SMEAR II station via ACTRIS-
872 HY.

873

Tables

Table 1 Overview of the simulation input parameters that remain unchanged in all of the simulation sets conducted with or without co-condensation. The updraft velocities, organic volatility distributions and vapor concentrations that change between simulation sets are reported in Table 2 together with the median model outputs. The time series of these model input data are shown in Fig.1. All the modelling scenarios are initiated at 90% relative humidity.

Parameter	Min	Max	Median
Aitken mode number conc. N_1 [cm^{-3}] [a]	160	12 316	1491
Accumulation mode number conc. N_2 [cm^{-3}] [a]	44	2 433	560
Aitken mode geometric mean dry diameter D_1 [nm] [a]	7.1	71.0	23.8
Accumulation mode geometric mean dry diameter D_2 [nm] [a]	62.6	201.9	115.3
Geom. standard deviation of Aitken mode σ_1 [a]	1.50	2.08	1.75
Geom. standard deviation of accumulation mode σ_2 [a]	1.33	2.06	1.75
Number of PNSD size bins	400	400	400
Organic mass fraction f_{Org} [%] [b]	25	84	68
Initial T [K] [c]	271	295	279
Initial p [hPa]	980	980	980
Mass accommodation coefficient α	1	1	1
Effective soluble fraction of organics	1	1	1
Surface tension γ [mN m^{-1}]	72.8	72.8	72.8
ICPM time step [s]	10^{-3}	10^{-3}	10^{-3}

[a] Retrieved from fits assigned onto the measured aerosol size distributions (Aalto et al., 2001) using a fitting algorithm by Hussein et al. (2005).
[b] Retrieved from aerosol chemical composition measurements (Heikkinen et al., 2020).
[c] Retrieved from radio soundings (ARM Data Center, 2014). The temperatures shown were recorded when the relative humidity measured by the radiosonde reached 90%, i.e., the initial relative humidity used for the adiabatic ascents.

Table 2 Overview of the simulation output for the no co-condensation (noCC) and co-condensation (CC) simulations performed using varying updraft velocities.

Parameter	Median values			
Volatility distribution [a]	F	CJ	F	F
Updraft velocity w [m s^{-1}] [a]	0.1	0.3	0.3	1.0
Parcel displacement before CB [m]	190	190	190	190
Cloud droplet number conc. CDNC$_{noCC}$ [cm^{-3}] [b]	161	300	300	530
Cloud droplet number conc. CDNC$_{CC}$ [cm^{-3}] [b]	190	358	411	645
CDNC enhancement ΔCDNC [%] [b]	16.8	12.4	23.3	20.6
Maximum supersaturation s_{max}^{noCC} [%]	0.15	0.24	0.24	0.41
Maximum supersaturation s_{max}^{CC} [%]	0.14	0.23	0.22	0.38
Smallest activated dry radius r_{noCC}^{*} [nm]	71.9	50.9	50.9	36.0
Smallest activated dry radius r_{CC}^{*} [nm]	63.7	46.7	44.3	30.3
Initial organic vapor conc. $\sum c_g^{INIT}$ [µg m^{-3}]	1.99	1.07	1.99	1.99
Organic vapor condensed below cloud base $\sum c_g^{INIT} - \sum c_g^{CB}$ [µg m^{-3}]	1.81	0.66	1.43	0.69
Fraction of organic vapor condensed below cloud base $\Delta C_g^{INIT \rightarrow CB}$ [%]	91.0	61.7	71.9	34.7

[a] Model input parameters crucial for understanding the differences between the co-condensation simulation model outputs.
[b] The CDNC represent the integrated number concentration in size bins exceeding the critical radius in size at 50 meters above cloud base (CB).
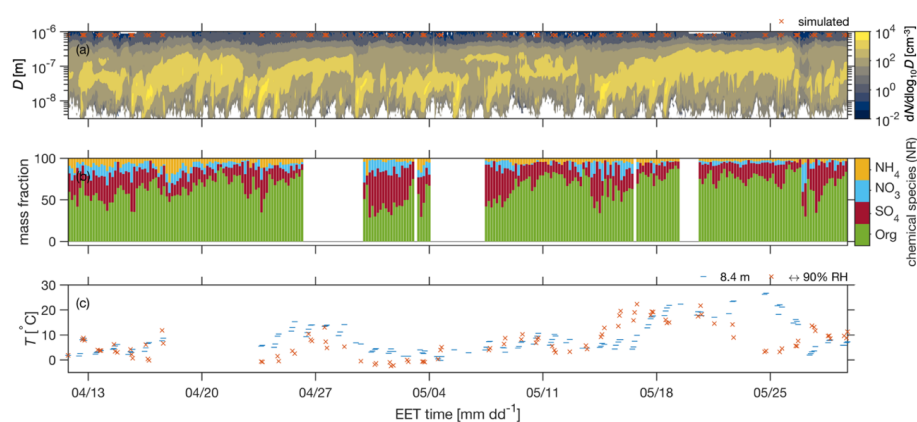
Figures

Figure 1 (**a**) Time-series of the particle number size distribution in the time period of interest during BAECC. The time points used for the ICPM initialization are shown as orange crosses. (**b**) The non-refractory (NR) chemical composition of sub-micrometer aerosol particles for the same time period. (**c**) The time series of ambient temperature near ground level (8.4 m a.g.l.) is shown in blue and the ICPM initialization temperature corresponding to RH = 90% from the interpolated radiosonde data product is shown in orange. The subpanels have a common x–axis representing the East European winter time (UTC+2).

902
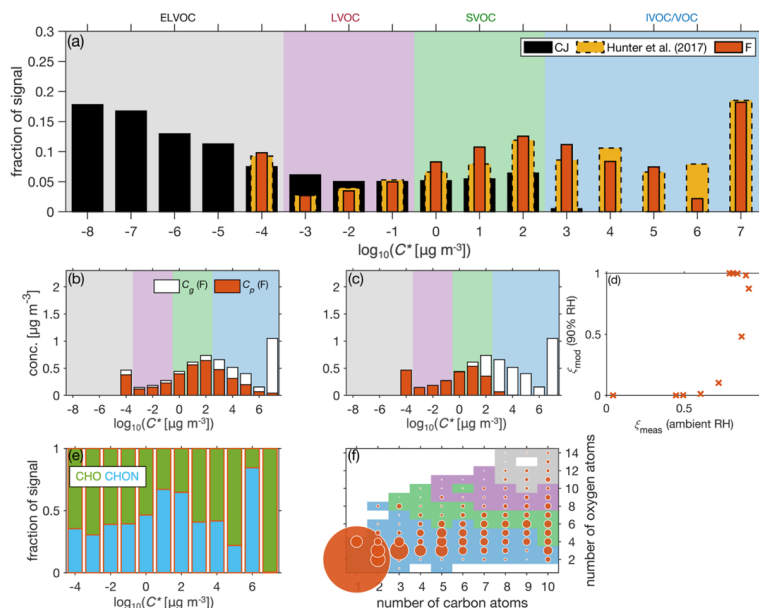
903
904
905 **Figure 2 (a)** The normalized volatility distributions ($C_g + C_p$) from Cappa and Jimenez (2010; CJ) and the BAECC FIGAERO-
906 I-CIMS measurements (F) using the modified Li et al. (2016) molecular formulae-based parameterizations. A volatility
907 distribution from Hunter et al. (2017) constructed from the BEACHON-RoMBAS measurement campaign in shown in the
908 dashed bars. The volatility ranges for ELVOC, LVOC, SVOC and IVOC/VOC are shown in color scales. These C^* limits
909 apply throughout the paper. **(b–c)** The partitioning predicted based on the FIGAERO-I-CIMS gas- and particle-phase
910 measurements and the ICPM, respectively. **(d)** A scatterplot drawn between the FIGAERO-I-CIMS derived partitioning
911 coefficients (ξ_{meas}) and ICPM derived coefficients (ξ_{mod}) for the 12 different volatility bins. Panels **(e–f)** represent the gas phase
912 molecular composition from the FIGAERO-I-CIMS: panel **(e)** the distribution between organic nitrates and non-nitrates and
913 panel **(f)** the degree of oxygenation in the form of oxygen and carbon numbers. The marker size in panel **f** corresponds to the
914 concentration of signal for the given n_C and n_O combination.

915
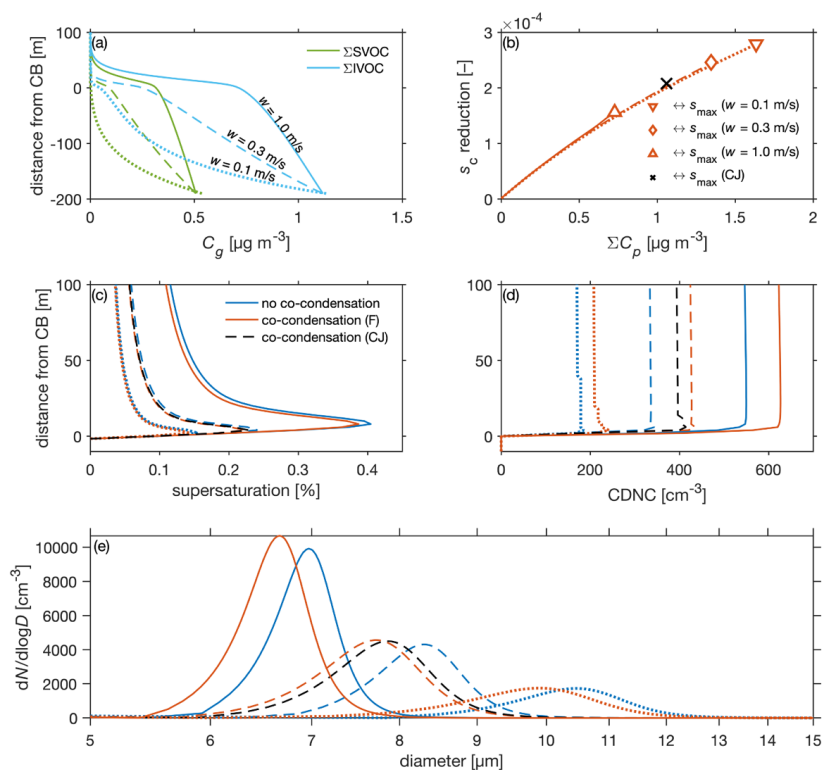
Figure 3 A summary of simulated cloud microphysics on May 11, 11:30 EET during the BAECC campaign. Simulations are
performed both with and without organic condensation (red and blue lines, respectively) for three different updraft velocities
(see line styles from panel **a**). The initial temperature is 279 K, pressure 980 hPa and supersaturation –0.1% (RH = 90%). (**a**)
The concentration of SVOCs and IVOCs in the gas phase as a function of distance from cloud base (CB). (**b**) The absolute
change in critical supersaturation as a function of soluble mass added along the ascent by condensing organics. The markers
represent the reductions at the maximum supersaturation (s_{max}). (**c–d**) The evolution of the s_{max} and CDNC with altitude,
respectively. (**e**) The droplet spectra 50 meters above CB. Size bins exceeding the critical diameter as predicted by Köhler
theory are calculated as cloud droplets. The red lines are obtained with F volatility distributions and the black with CJ (**Fig.
2a**). The line type specifications in panels **d–e** follow those shown in panel **a** and the colors used in panels **d–e** are documented
in the panel **c** legend.

926
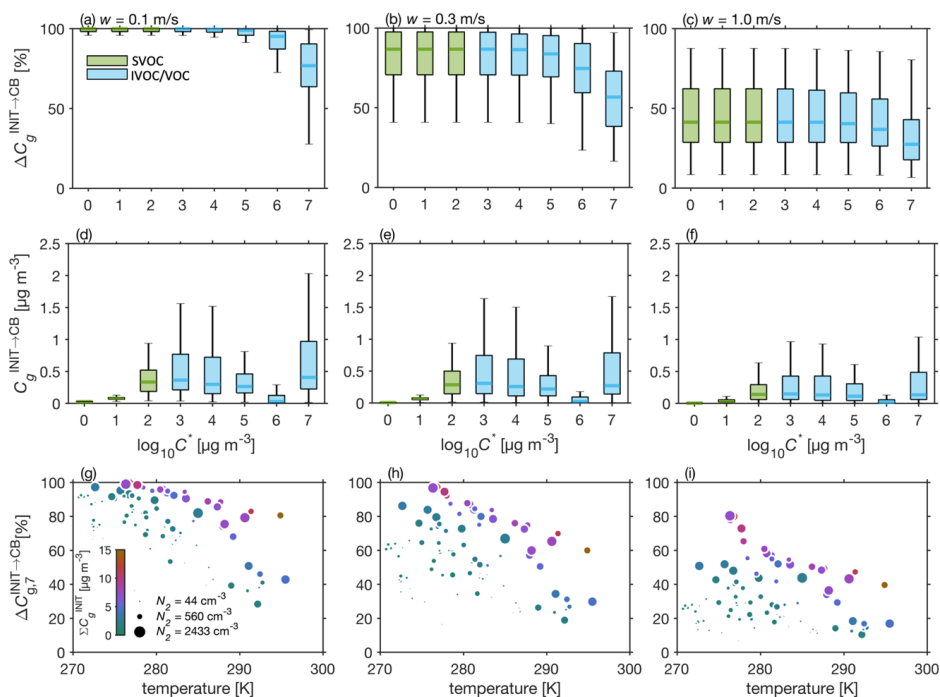
Figure 4 Box plots showing the fractions (**a–c**) and absolute concentrations (**d–f**) of vapor condensed below cloud base per
volatility bin for the 0.1, 0.3 and 1.0 m s^{-1} updraft scenarios, respectively. The volatility ranges in panels a–f start from $\log_{10}C^{*}$
= 0 because of the negligible gas-phase concentrations in the lower volatility bins. The final row (**g–i**) shows how the fraction
of vapor condensed from the highest volatility bin (y–axis) behaves as a function of ICPM initialization temperature (x–axis),
accumulation mode number concentration (marker size) and total initial organic vapor concentration (marker color).

927
928
929
930
931
932
933
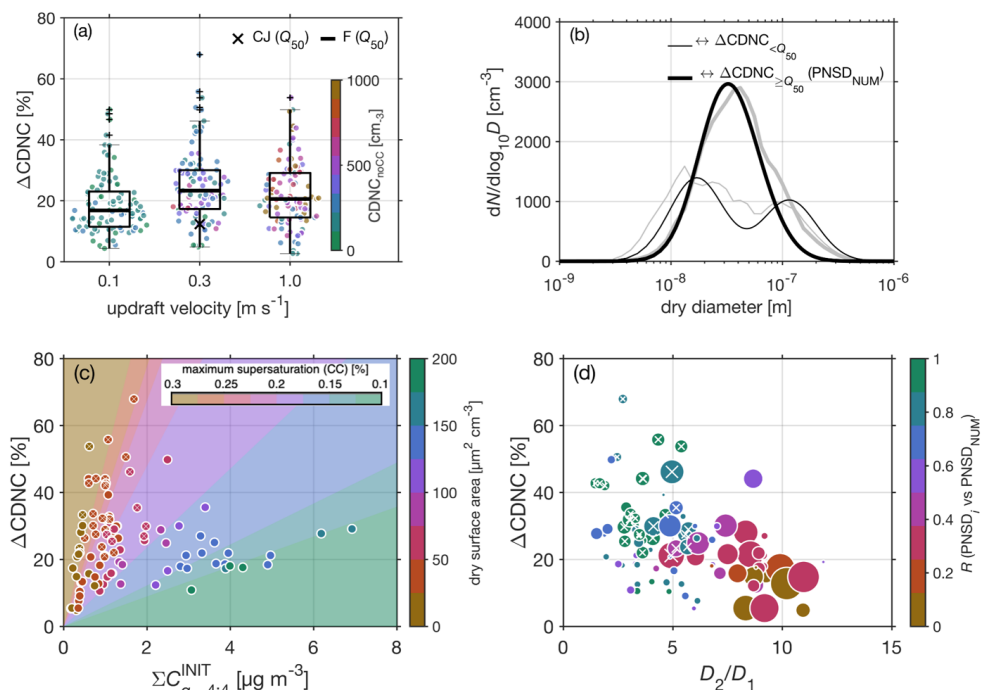
Figure 5 (**a**) Box plots showing the predicted ΔCDNC (using F volatility distributions) due to co-condensation in the three different modelling scenarios (0.1, 0.3 and 1.0 m s^{-1} updrafts). The median (Q_{50}) ΔCDNC yielded using the CJ distribution is shown with a black cross. The colorful markers represent CDNC (without accounting for co-condensation) in form of a swarmplot. (**b**) The median initial dry size distributions calculated from the simulations exceeding the 75th percentile in ΔCDNC ($\leftrightarrow Q_{75}$; thick lines) and remaining below the 25th percentile ($\leftrightarrow Q_{25}$; thin lines), respectively. The median is calculated by taking a median of the log-normal parameters from both sets of simulations (in black) and from the measurement data (in grey). The data are shown for the simulation performed with a 0.3 m s^{-1} updraft. The black lines are drawn from the ICPM input modal parameters and the grey lines from the measured size distribution data. (**c**) The relationship between the modeled ΔCDNC and the initial organic vapor concentration within the $\log_{10} C^*$ range from -4 to 4 ($C_{g,\,-4:4}^{INIT}$). The marker color-coding represents the initial dry size distribution surface area (A). The plot background is colored with the modeled maximum supersaturations (s_{max}). These are calculated from s_{max} binned ΔCDNC vs $C_{g,\,-4:4}^{INIT}$ linear fit 90% confidence intervals (CI; area between CI is colored). The figure shows that A anticorrelates with s_{max} (see Eq. 3). The data are shown for the simulations performed with a 0.3 m s^{-1} updraft only.
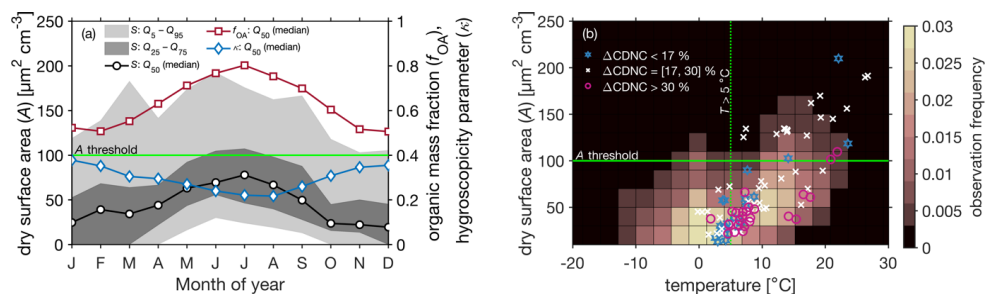
Figure 6 (a) The seasonal cycle of the dry aerosol size distribution surface area (S) calculated from the long-term aerosol size distribution observations (2012–2017; left y-axis), where the markers represent the median values, the darkest shading the interquartile range and the lighter shading the area between the 5th and 95th percentiles. The panel also contains the median seasonal cycles of organic mass fraction and the κ hygroscopicity parameter compiled from the same long-term period (right y-axis). The green horizontal line refers to the dry surface area threshold of 100 µm^2 cm^{-3} from Fig. 5, under which the greatest ΔCDNC are modeled using the BAECC data. **(b)** A density plot showing the observations of S under different ambient temperatures during the 2012–2017 long-term period. The A threshold of 100 µm^2 cm^{-3} is again shown with the horizontal green line. The vertical dashed green line is a rough estimate for the start of the thermal growing season, which also refers to the starting point of the majority of the BVOC emissions. The markers show the ICPM simulation data color-coded with the associated ΔCDNC (simulations yielding the ΔCDNC below the 25th percentile are shown in blue, simulations yielding ΔCDNC above the 75th percentile in red and the simulations between those limits are shown in white).
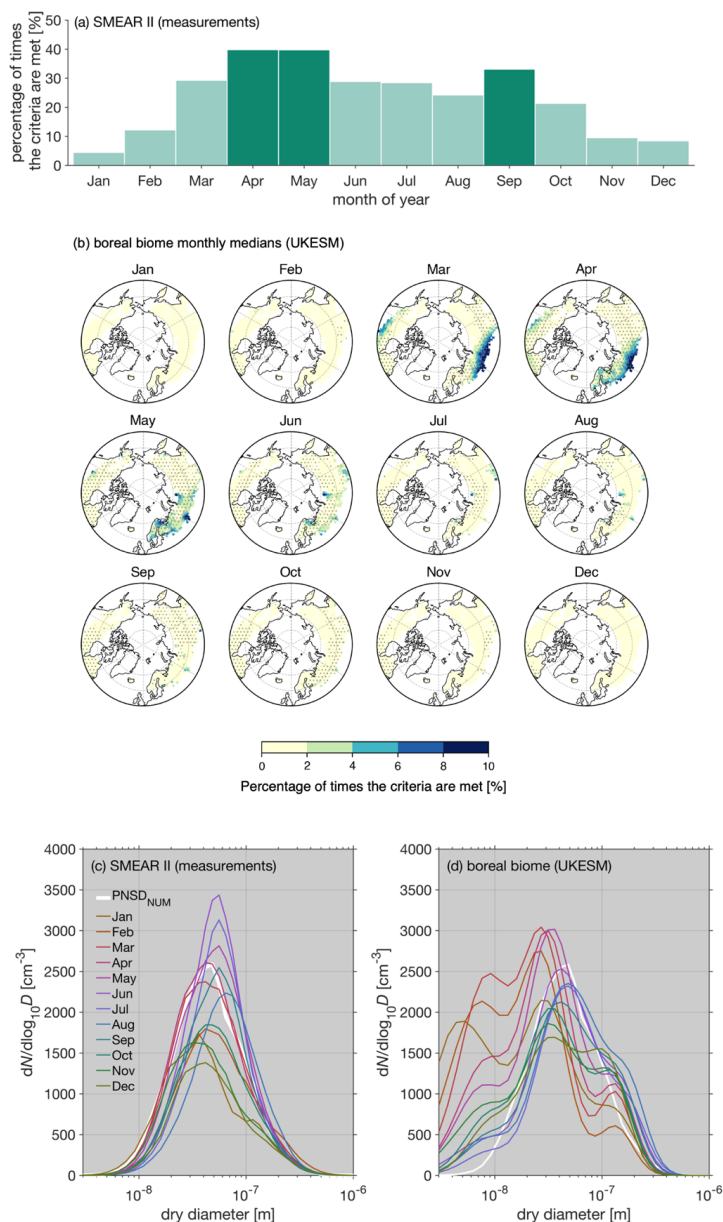
Figure 7 (a) Percentage of times the criteria (D_2/D_1<6 and N_1>1000 cm^{-3}) are met at SMEAR II between the 2012–2017 measurement period. D_2, D_1 and N_1 are attained from bimodal fits calculated for the measured PNSD using the Hussein et al. (2005) algorithm. **(b)** The percentage of times the criteria are met in a 2009–2013 UKESM1 simulation. D_2, D_1 and N_1 are the modal parameters representing the soluble accumulation mode and soluble Aitken mode parameters. The gray markers refer to boreal grid cells, where the median updraft velocity at cloud base is between 0.2 and 0.5 m s^{-1}. **(c–d)** Monthly median size distributions from the long-term PNSD measurements at SMEAR II and UKESM1 simulation, respectively. The UKESM1 size distributions are calculated from the log-normal PNSD parameters for nucleation, soluble Aitken and soluble accumulation modes assuming geometric standard deviations of $\sigma = 1.59$ for nucleation and soluble Aitken modes and $\sigma = 1.4$ for the soluble accumulation mode. The soluble coarse mode is not included in the analysis.

References

Aalto, P., Hämeri, K., Becker, E., Weber, R., Salm, J., Mäkelä, J. M., Hoell, C., O'dowd, C. D., Hansson, H.-C., Väkevä, M., Koponen, I. K., Buzorius, G., and Kulmala, M.: Physical characterization of aerosol particles during nucleation events, Tellus B: Chemical and Physical Meteorology, 53, 344–358, https://doi.org/10.3402/tellusb.v53i4.17127, 2001.

Allan, J. D., Alfarra, M. R., Bower, K. N., Coe, H., Jayne, J. T., Worsnop, D. R., Aalto, P. P., Kulmala, M., Hyötyläinen, T., Cavalli, F., and Laaksonen, A.: Size and composition measurements of background aerosol and new particle growth in a Finnish forest during QUEST 2 using an Aerodyne Aerosol Mass Spectrometer, Atmos. Chem. Phys., 6, 315–327, https://doi.org/10.5194/acp-6-315-2006, 2006.

AeroCom: https://aerocom.met.no/, last access: 21 November 2022.

ARM Data Center: Atmospheric Radiation Measurement (ARM) user facility. 2014, updated hourly. Interpolated Sonde (INTERPOLATEDSONDE). 2014-04-01 to 2014-07-01, ARM Mobile Facility (TMP) U. of Helsinki Research Station (SMEAR II), Hyytiala, Finland; AMF2 (M1). Compiled by M. Jensen, S. Giangrande, T. Fairless and A. Zhou., 2014.

Artaxo, P., Hansson, H.-C., Andreae, M. O., Bäck, J., Alves, E. G., Barbosa, H. M. J., Bender, F., Bourtsoukidis, E., Carbone, S., Chi, J., Decesari, S., Després, V. R., Ditas, F., Ezhova, E., Fuzzi, S., Hasselquist, N. J., Heintzenberg, J., Holanda, B. A., Guenther, A., Hakola, H., Heikkinen, L., Kerminen, V.-M., Kontkanen, J., Krejci, R., Kulmala, M., Lavric, J. V., Leeuw, G. de, Lehtipalo, K., Machado, L. A. T., McFiggans, G., Franco, M. A. M., Meller, B. B., Morais, F. G., Mohr, C., Morgan, W., Nilsson, M. B., Peichl, M., Petäjä, T., Praß, M., Pöhlker, C., Pöhlker, M. L., Pöschl, U., Randow, C. V., Riipinen, I., Rinne, J., Rizzo, L. V., Rosenfeld, D., Dias, M. A. F. S., Sogacheva, L., Stier, P., Swietlicki, E., Sörgel, M., Tunved, P., Virkkula, A., Wang, J., Weber, B., Yáñez-Serrano, A. M., Zieger, P., Mikhailov, E., Smith, J. N., and Kesselmeier, J.: Tropical and Boreal Forest – Atmosphere Interactions: A Review, Tellus B: Chemical and Physical Meteorology, 74, 24–163, https://doi.org/10.16993/tellusb.34, 2022.

Bardakov, R., Riipinen, I., Krejci, R., Savre, J., Thornton, J. A., and Ekman, A. M. L.: A Novel Framework to Study Trace Gas Transport in Deep Convective Clouds, Journal of Advances in Modeling Earth Systems, 12, e2019MS001931, https://doi.org/10.1029/2019MS001931, 2020.

Bellouin, N., Quaas, J., Gryspeerdt, E., Kinne, S., Stier, P., Watson-Parris, D., Boucher, O., Carslaw, K. S., Christensen, M., Daniau, A.-L., Dufresne, J.-L., Feingold, G., Fiedler, S., Forster, P., Gettelman, A., Haywood, J. M., Lohmann, U., Malavelle, F., Mauritsen, T., McCoy, D. T., Myhre, G., Mülmenstädt, J., Neubauer, D., Possner, A., Rugenstein, M., Sato, Y., Schulz, M., Schwartz, S. E., Sourdeval, O., Storelvmo, T., Toll, V., Winker, D., and Stevens, B.: Bounding Global Aerosol Radiative Forcing of Climate Change, Reviews of Geophysics, 58, e2019RG000660, https://doi.org/10.1029/2019RG000660, 2020.

Birmili, W., Stopfkuchen, K., Hermann, M., Wiedensohler, A., and Heintzenberg, J.: Particle Penetration Through a 300 m Inlet Pipe for Sampling Atmospheric Aerosols from a Tall Meteorological Tower, Aerosol Science and Technology, 41, 811–817, https://doi.org/10.1080/02786820701484948, 2007.

Boucher, O., Randall, D., Artaxo, P., Bretherton, C., Feingold, G., Forster, P., Kerminen, V.-M., Kondo, Y., Liao, H., Lohmann, U., Rasch, P., Satheesh, S. K., Sherwood, S., Stevens, B., Zhang, X. Y., Stocker, T. F., Qin, D., Plattner, G.-K., Tignor, M., Allen, S. K., Boschung, J., Nauels, A., Xia, Y., Bex, V., and Midgley, P. M.: Clouds and Aerosols. In: Climate Change 2013: The Physical Science Basis. Contribution of Working Group I to the Fifth Assessment Report of the Intergovernmental Panel on Climate Change, Cambridge University Press, 2013.

Canagaratna, M. r., Jayne, J. t., Jimenez, J. l., Allan, J. d., Alfarra, M. r., Zhang, Q., Onasch, T. b., Drewnick, F., Coe, H., Middlebrook, A., Delia, A., Williams, L. r., Trimborn, A. m., Northway, M. j., DeCarlo, P. f., Kolb, C. e., Davidovits, P., and Worsnop, D. r.: Chemical and microphysical

1023   characterization of ambient aerosols with the aerodyne aerosol mass spectrometer, Mass
1024   Spectrometry Reviews, 26, 185–222, https://doi.org/10.1002/mas.20115, 2007.

1025   Cappa, C. D.: A model of aerosol evaporation kinetics in a thermodenuder, Atmos. Meas. Tech., 3,
1026   579–592, https://doi.org/10.5194/amt-3-579-2010, 2010.

1027   Cappa, C. D. and Jimenez, J. L.: Quantitative estimates of the volatility of ambient organic aerosol,
1028   Atmos. Chem. Phys., 10, 5409–5424, https://doi.org/10.5194/acp-10-5409-2010, 2010.

1029   Carslaw, K. S., Lee, L. A., Reddington, C. L., Pringle, K. J., Rap, A., Forster, P. M., Mann, G. W.,
1030   Spracklen, D. V., Woodhouse, M. T., Regayre, L. A., and Pierce, J. R.: Large contribution of natural
1031   aerosols to uncertainty in indirect forcing, Nature, 503, 67–71, https://doi.org/10.1038/nature12674,
1032   2013.

1033   Cerully, K. M., Raatikainen, T., Lance, S., Tkacik, D., Tiitta, P., Petäjä, T., Ehn, M., Kulmala, M.,
1034   Worsnop, D. R., Laaksonen, A., Smith, J. N., and Nenes, A.: Aerosol hygroscopicity and CCN
1035   activation kinetics in a boreal forest environment during the 2007 EUCAARI campaign, Atmospheric
1036   Chemistry and Physics, 11, 12369–12386, https://doi.org/10.5194/acp-11-12369-2011, 2011.

1037   Crooks, M., Connolly, P., and McFiggans, G.: A parameterisation for the co-condensation of semi-
1038   volatile organics into multiple aerosol particle modes, Geosci. Model Dev., 11, 3261–3278,
1039   https://doi.org/10.5194/gmd-11-3261-2018, 2018.

1040   Dada, L., Paasonen, P., Nieminen, T., Buenrostro Mazon, S., Kontkanen, J., Peräkylä, O., Lehtipalo,
1041   K., Hussein, T., Petäjä, T., Kerminen, V.-M., Bäck, J., and Kulmala, M.: Long-term analysis of clear-
1042   sky new particle formation events and nonevents in Hyytiälä, Atmos. Chem. Phys., 17, 6227–6241,
1043   https://doi.org/10.5194/acp-17-6227-2017, 2017.

1044   Daumit, K. E., Kessler, S. H., and Kroll, J. H.: Average chemical properties and potential formation
1045   pathways of highly oxidized organic aerosol, Faraday Discuss., 165, 181–202,
1046   https://doi.org/10.1039/C3FD00045A, 2013.

1047   Donahue, N. M., Robinson, A. L., Stanier, C. O., and Pandis, S. N.: Coupled Partitioning, Dilution, and
1048   Chemical Aging of Semivolatile Organics, Environ. Sci. Technol., 40, 2635–2643,
1049   https://doi.org/10.1021/es052297c, 2006.

1050   Donahue, N. M., Epstein, S. A., Pandis, S. N., and Robinson, A. L.: A two-dimensional volatility basis
1051   set: 1. organic-aerosol mixing thermodynamics, Atmos. Chem. Phys., 11, 3303–3318,
1052   https://doi.org/10.5194/acp-11-3303-2011, 2011.

1053   Epstein, S. A., Riipinen, I., and Donahue, N. M.: A Semiempirical Correlation between Enthalpy of
1054   Vaporization and Saturation Concentration for Organic Aerosol, Environ. Sci. Technol., 44, 743–748,
1055   https://doi.org/10.1021/es902497z, 2010.

1056   Forster, P., Storelvmo, T., Armour, K., Collins, W., Dufresne, J.-L., Frame, D., Lunt, D. J., Mauritsen,
1057   T., Palmer, M. D., Watanabe, M., Wild, M., and Zhang, H.: The Earth's energy budget, climate
1058   feedbacks, and climate sensitivity, in: Climate Change 2021: The Physical Science Basis.
1059   Contribution of Working Group I to the Sixth Assessment Report of the Intergovernmental Panel on
1060   Climate Change, edited by: Masson-Delmotte, V., Zhai, P., Pirani, A., Connors, S. L., Péan, C.,
1061   Berger, S., Caud, N., Chen, Y., Goldfarb, L., Gomis, M. I., Huang, M., Leitzell, K., Lonnoy, E.,
1062   Matthews, J. B. R., Maycock, T. K., Waterfield, T., Yelekçi, Ö., Yu, R., and Zhou, B., Cambridge
1063   University Press, 2021.

1064   Fredenslund, A., Jones, R. L., and Prausnitz, J. M.: Group-contribution estimation of activity
1065   coefficients in nonideal liquid mixtures, AIChE Journal, 21, 1086–1099,
1066   https://doi.org/10.1002/aic.690210607, 1975.

1067   Galloway, J. N., Likens, G. E., Keene, W. C., and Miller, J. M.: The composition of precipitation in
1068   remote areas of the world, Journal of Geophysical Research: Oceans, 87, 8771–8786,
1069   https://doi.org/10.1029/JC087iC11p08771, 1982.

1070   Graham, E. L., Wu, C., Bell, D. M., Bertrand, A., Haslett, S. L., Baltensperger, U., El Haddad, I.,
1071   Krejci, R., Riipinen, I., and Mohr, C.: Volatility of aerosol particles from NO$_3$ oxidation of various
1072   biogenic organic precursors, EGUsphere, 1–22, https://doi.org/10.5194/egusphere-2022-1043, 2022.

1073   Guenther, A., Hewitt, C. N., Erickson, D., Fall, R., Geron, C., Graedel, T., Harley, P., Klinger, L.,
1074   Lerdau, M., Mckay, W. A., Pierce, T., Scholes, B., Steinbrecher, R., Tallamraju, R., Taylor, J., and
1075   Zimmerman, P.: A global model of natural volatile organic compound emissions, Journal of
1076   Geophysical Research: Atmospheres, 100, 8873–8892, https://doi.org/10.1029/94JD02950, 1995.

1077   Guenther, A. B., Zimmerman, P. R., Harley, P. C., Monson, R. K., and Fall, R.: Isoprene and
1078   monoterpene emission rate variability: Model evaluations and sensitivity analyses, Journal of
1079   Geophysical Research: Atmospheres, 98, 12609–12617, https://doi.org/10.1029/93JD00527, 1993.

1080   Hakola, H., Hellén, H., Hemmilä, M., Rinne, J., and Kulmala, M.: In situ measurements of volatile
1081   organic compounds in a boreal forest, Atmos. Chem. Phys., 12, 11665–11678,
1082   https://doi.org/10.5194/acp-12-11665-2012, 2012.

1083   Hallquist, M., Wenger, J. C., Baltensperger, U., Rudich, Y., Simpson, D., Claeys, M., Dommen, J.,
1084   Donahue, N. M., George, C., Goldstein, A. H., Hamilton, J. F., Herrmann, H., Hoffmann, T., Iinuma,
1085   Y., Jang, M., Jenkin, M. E., Jimenez, J. L., Kiendler-Scharr, A., Maenhaut, W., McFiggans, G., Mentel,
1086   T. F., Monod, A., Prévôt, A. S. H., Seinfeld, J. H., Surratt, J. D., Szmigielski, R., and Wildt, J.: The
1087   formation, properties and impact of secondary organic aerosol: current and emerging issues,
1088   Atmospheric Chemistry and Physics, 9, 5155–5236, https://doi.org/10.5194/acp-9-5155-2009, 2009.

1089   Hänel, G.: The role of aerosol properties during the condensational stage of cloud: A reinvestigation
1090   of numerics and microphysics, Beitr. Phys. Atmos., 60, 321–339, 1987.

1091   Hari, P. and Kulmala, M.: Station for Measuring Ecosystem–Atmosphere Relations (SMEAR II),
1092   Boreal Environ. Res., 10, 8, 2005.

1093   Hegg, D. A.: Impact of gas-phase HNO3 and NH3 on microphysical processes in atmospheric clouds,
1094   Geophysical Research Letters, 27, 2201–2204, https://doi.org/10.1029/1999GL011252, 2000.

1095   Heikkinen, L., Äijälä, M., Riva, M., Luoma, K., Daellenbach, K., Aalto, J., Aalto, P., Aliaga, D., Aurela,
1096   M., Keskinen, H., Makkonen, U., Rantala, P., Kulmala, M., Petäjä, T., Worsnop, D., and Ehn, M.:
1097   Long-term sub-micrometer aerosol chemical composition in the boreal forest: inter- and intra-annual
1098   variability, Atmos. Chem. Phys., 20, 3151–3180, https://doi.org/10.5194/acp-20-3151-2020, 2020.

1099   Heikkinen, L., Äijälä, M., Daellenbach, K. R., Chen, G., Garmash, O., Aliaga, D., Graeffe, F., Räty, M.,
1100   Luoma, K., Aalto, P., Kulmala, M., Petäjä, T., Worsnop, D., and Ehn, M.: Eight years of sub-
1101   micrometre organic aerosol composition data from the boreal forest characterized using a machine-
1102   learning approach, Atmos. Chem. Phys., 21, 10081–10109, https://doi.org/10.5194/acp-21-10081-
1103   2021, 2021.

1104   Hong, J., Häkkinen, S. a. K., Paramonov, M., Äijälä, M., Hakala, J., Nieminen, T., Mikkilä, J., Prisle, N.
1105   L., Kulmala, M., Riipinen, I., Bilde, M., Kerminen, V.-M., and Petäjä, T.: Hygroscopicity, CCN and
1106   volatility properties of submicron atmospheric aerosol in a boreal forest environment during the
1107   summer of 2010, Atmospheric Chemistry and Physics, 14, 4733–4748, https://doi.org/10.5194/acp-
1108   14-4733-2014, 2014.

1109   Hoppel, W. A. and Frick, G. M.: Submicron aerosol size distributions measured over the tropical and
1110   South Pacific, Atmospheric Environment. Part A. General Topics, 24, 645–659,
1111   https://doi.org/10.1016/0960-1686(90)90020-N, 1990.

1112   Hu, D., Topping, D., and McFiggans, G.: Measured particle water uptake enhanced by co-condensing
1113   vapours, Atmospheric Chemistry and Physics, 18, 14925–14937, https://doi.org/10.5194/acp-18-
1114   14925-2018, 2018.

1115   Huang, W., Li, H., Sarnela, N., Heikkinen, L., Tham, Y. J., Mikkilä, J., Thomas, S. J., Donahue, N. M.,
1116   Kulmala, M., and Bianchi, F.: Measurement report: Molecular composition and volatility of gaseous

1117   organic compounds in a boreal forest – from volatile organic compounds to highly oxygenated organic
1118   molecules, Atmos. Chem. Phys., 21, 8961–8977, https://doi.org/10.5194/acp-21-8961-2021, 2021.

1119   Huffman, J. A., Docherty, K. S., Aiken, A. C., Cubison, M. J., Ulbrich, I. M., DeCarlo, P. F., Sueper, D.,
1120   Jayne, J. T., Worsnop, D. R., Ziemann, P. J., and Jimenez, J. L.: Chemically-resolved aerosol
1121   volatility measurements from two megacity field studies, Atmos. Chem. Phys., 9, 7161–7182,
1122   https://doi.org/10.5194/acp-9-7161-2009, 2009a.

1123   Huffman, J. A., Docherty, K. S., Mohr, C., Cubison, M. J., Ulbrich, I. M., Ziemann, P. J., Onasch, T. B.,
1124   and Jimenez, J. L.: Chemically-Resolved Volatility Measurements of Organic Aerosol from Different
1125   Sources, Environ. Sci. Technol., 43, 5351–5357, https://doi.org/10.1021/es803539d, 2009b.

1126   Hunter, J. F., Day, D. A., Palm, B. B., Yatavelli, R. L. N., Chan, A. W. H., Kaser, L., Cappellin, L.,
1127   Hayes, P. L., Cross, E. S., Carrasquillo, A. J., Campuzano-Jost, P., Stark, H., Zhao, Y., Hohaus, T.,
1128   Smith, J. N., Hansel, A., Karl, T., Goldstein, A. H., Guenther, A., Worsnop, D. R., Thornton, J. A.,
1129   Heald, C. L., Jimenez, J. L., and Kroll, J. H.: Comprehensive characterization of atmospheric organic
1130   carbon at a forested site, Nature Geosci, 10, 748–753, https://doi.org/10.1038/ngeo3018, 2017.

1131   Hussein, T., Maso, M. D., Petäjä, T., Koponen, I. K., Paatero, P., Aalto, P. P., Hämeri, K., and
1132   Kulmala, M.: Evaluation of an automatic algorithm for fitting the particle number size distributions,
1133   Boreal Environ. Res., 10, 19, 2005.

1134   Isaacman-VanWertz, G. and Aumont, B.: Impact of organic molecular structure on the estimation of
1135   atmospherically relevant physicochemical parameters, Atmos. Chem. Phys., 21, 6541–6563,
1136   https://doi.org/10.5194/acp-21-6541-2021, 2021.

1137   Kakavas, S., Pandis, S. N., and Nenes, A.: ISORROPIA-Lite: A Comprehensive Atmospheric Aerosol
1138   Thermodynamics Module for Earth System Models, Tellus B: Chemical and Physical Meteorology, 74,
1139   1–23, https://doi.org/10.16993/tellusb.33, 2022.

1140   Karnezi, E., Riipinen, I., and Pandis, S. N.: Measuring the atmospheric organic aerosol volatility
1141   distribution: a theoretical analysis, Atmos. Meas. Tech., 7, 2953–2965, https://doi.org/10.5194/amt-7-
1142   2953-2014, 2014.

1143   Kerminen, V.-M., Chen, X., Vakkari, V., Petäjä, T., Kulmala, M., and Bianchi, F.: Atmospheric new
1144   particle formation and growth: review of field observations, Environ. Res. Lett., 13, 103003,
1145   https://doi.org/10.1088/1748-9326/aadf3c, 2018.

1146   Köhler, H.: The nucleus in and the growth of hygroscopic droplets, Trans. Faraday Soc., 32, 1152–
1147   1161, https://doi.org/10.1039/TF9363201152, 1936.

1148   Kontkanen, J., Paasonen, P., Aalto, J., Bäck, J., Rantala, P., Petäjä, T., and Kulmala, M.: Simple
1149   proxies for estimating the concentrations of monoterpenes and their oxidation products at a boreal
1150   forest site, Atmospheric Chemistry and Physics, 16, 13291–13307, https://doi.org/10.5194/acp-16-
1151   13291-2016, 2016.

1152   Korhonen, P., Kulmala, M., and Vesala, T.: Model simulation of the amount of soluble mass during
1153   cloud droplet formation, Atmospheric Environment, 30, 1773–1785, https://doi.org/10.1016/1352-
1154   2310(95)00380-0, 1996.

1155   Kulmala, M., Laaksonen, A., Korhonen, P., Vesala, T., Ahonen, T., and Barrett, J. C.: The effect of
1156   atmospheric nitric acid vapor on cloud condensation nucleus activation, Journal of Geophysical
1157   Research: Atmospheres, 98, 22949–22958, https://doi.org/10.1029/93JD02070, 1993.

1158   Kulmala, M., Rannik, Ü., Pirjola, L., Maso, M. D., Karimäki, J., Asmi, A., Jäppinen, A., Karhu, V.,
1159   Korhonen, H., Malvikko, S.-P., Puustinen, A., Raittila, J., Romakkaniemi, S., Suni, T., Yli-Koivisto, S.,
1160   Paatero, J., Hari, P., and Vesala, T.: Characterization of atmospheric trace gas and aerosol
1161   concentrations at forest sites in southern and northern Finland using back trajectories, Boreal Environ.
1162   Res., 5, 22, 2000.

1163 Kulmala, M., Suni, T., Lehtinen, K. E. J., Dal Maso, M., Boy, M., Reissell, A., Rannik, Ü., Aalto, P.,
1164 Keronen, P., Hakola, H., Bäck, J., Hoffmann, T., Vesala, T., and Hari, P.: A new feedback mechanism
1165 linking forests, aerosols, and climate, Atmospheric Chemistry and Physics, 4, 557–562,
1166 https://doi.org/10.5194/acp-4-557-2004, 2004.

1167 Kulmala, M., Nieminen, T., Nikandrova, A., Lehtipalo, K., Manninen, H. E., Kajos, M. K., Kolari, P.,
1168 Lauri, A., Petäjä, T., Krejci, R., Hansson, H.-C., Swietlicki, E., Lindroth, A., Christensen, T. R., Arneth,
1169 A., Hari, P., Bäck, J., Vesala, T., and Kerminen, V.-M.: CO2-induced terrestrial climate feedback
1170 mechanism: From carbon sink to aerosol source and back, Boreal Environ. Res., 19, 10, 2014.

1171 Kyrö, E.-M., Väänänen, R., Kerminen, V.-M., Virkkula, A., Petäjä, T., Asmi, A., Dal Maso, M.,
1172 Nieminen, T., Juhola, S., Shcherbinin, A., Riipinen, I., Lehtipalo, K., Keronen, P., Aalto, P. P., Hari, P.,
1173 and Kulmala, M.: Trends in new particle formation in eastern Lapland, Finland: effect of decreasing
1174 sulfur emissions from Kola Peninsula, Atmos. Chem. Phys., 14, 4383–4396,
1175 https://doi.org/10.5194/acp-14-4383-2014, 2014.

1176 Lee, B. H., Lopez-Hilfiker, F. D., D'Ambro, E. L., Zhou, P., Boy, M., Petäjä, T., Hao, L., Virtanen, A.,
1177 and Thornton, J. A.: Semi-volatile and highly oxygenated gaseous and particulate organic compounds
1178 observed above a boreal forest canopy, Atmos. Chem. Phys., 18, 11547–11562,
1179 https://doi.org/10.5194/acp-18-11547-2018, 2018.

1180 Lee, B. H., D'Ambro, E. L., Lopez-Hilfiker, F. D., Schobesberger, S., Mohr, C., Zawadowicz, M. A.,
1181 Liu, J., Shilling, J. E., Hu, W., Palm, B. B., Jimenez, J. L., Hao, L., Virtanen, A., Zhang, H., Goldstein,
1182 A. H., Pye, H. O. T., and Thornton, J. A.: Resolving Ambient Organic Aerosol Formation and Aging
1183 Pathways with Simultaneous Molecular Composition and Volatility Observations, ACS Earth Space
1184 Chem., 4, 391–402, https://doi.org/10.1021/acsearthspacechem.9b00302, 2020.

1185 Lee, I.-Y. and Pruppacher, H. R.: A comparative study on the growth of cloud drops by condensation
1186 using an air parcel model with and without entrainment, PAGEOPH, 115, 523–545,
1187 https://doi.org/10.1007/BF00876119, 1977.

1188 Li, Y., Pöschl, U., and Shiraiwa, M.: Molecular corridors and parameterizations of volatility in the
1189 chemical evolution of organic aerosols, Atmos. Chem. Phys., 16, 3327–3344,
1190 https://doi.org/10.5194/acp-16-3327-2016, 2016.

1191 Lohmann, U. and Feichter, J.: Global indirect aerosol effects: a review, Atmos. Chem. Phys., 23,
1192 2005.

1193 Lopez-Hilfiker, F. D., Mohr, C., Ehn, M., Rubach, F., Kleist, E., Wildt, J., Mentel, T. F., Lutz, A.,
1194 Hallquist, M., Worsnop, D., and Thornton, J. A.: A novel method for online analysis of gas and particle
1195 composition: description and evaluation of a Filter Inlet for Gases and AEROsols (FIGAERO), Atmos.
1196 Meas. Tech., 7, 983–1001, https://doi.org/10.5194/amt-7-983-2014, 2014.

1197 Lopez-Hilfiker, F. D., Mohr, C., Ehn, M., Rubach, F., Kleist, E., Wildt, J., Mentel, T. F., Carrasquillo, A.
1198 J., Daumit, K. E., Hunter, J. F., Kroll, J. H., Worsnop, D. R., and Thornton, J. A.: Phase partitioning
1199 and volatility of secondary organic aerosol components formed from α-pinene ozonolysis and OH
1200 oxidation: the importance of accretion products and other low volatility compounds, Atmospheric
1201 Chemistry and Physics, 15, 7765–7776, https://doi.org/10.5194/acp-15-7765-2015, 2015.

1202 Lowe, S. J.: Modelling the effects of organic aerosol phase partitioning processes on cloud formation,
1203 PhD thesis, Stockholm University, Faculty of Science, Department of Environmental Science,
1204 Stockholm, Sweden, 2020.

1205 Lowe, S. J., Partridge, D. G., Davies, J. F., Wilson, K. R., Topping, D., and Riipinen, I.: Key drivers of
1206 cloud response to surface-active organics, Nat Commun, 10, 5214, https://doi.org/10.1038/s41467-
1207 019-12982-0, 2019.

1208 Luoma, K.: AEROSOL OPTICAL PROPERTIES, BLACK CARBON AND THEIR SPATIO-TEMPORAL
1209 VARIATION, PhD thesis, University of Helsinki, 2021.

1210 Lutz, A., Mohr, C., Le Breton, M., Lopez-Hilfiker, F. D., Priestley, M., Thornton, J. A., and Hallquist,
1211 M.: Gas to Particle Partitioning of Organic Acids in the Boreal Atmosphere, ACS Earth Space Chem.,
1212 3, 1279–1287, https://doi.org/10.1021/acsearthspacechem.9b00041, 2019.

1213 Mann, G. W., Carslaw, K. S., Spracklen, D. V., Ridley, D. A., Manktelow, P. T., Chipperfield, M. P.,
1214 Pickering, S. J., and Johnson, C. E.: Description and evaluation of GLOMAP-mode: a modal global
1215 aerosol microphysics model for the UKCA composition-climate model, Geoscientific Model
1216 Development, 3, 519–551, https://doi.org/10.5194/gmd-3-519-2010, 2010.

1217 Mikhailov, E. F., Mironova, S., Mironov, G., Vlasenko, S., Panov, A., Chi, X., Walter, D., Carbone, S.,
1218 Artaxo, P., Heimann, M., Lavric, J., Pöschl, U., and Andreae, M. O.: Long-term measurements (2010–
1219 2014) of carbonaceous aerosol and carbon monoxide at the Zotino Tall Tower Observatory (ZOTTO)
1220 in central Siberia, Atmos. Chem. Phys., 17, 14365–14392, https://doi.org/10.5194/acp-17-14365-
1221 2017, 2017.

1222 Millet, D. B., Baasandorj, M., Farmer, D. K., Thornton, J. A., Baumann, K., Brophy, P., Chaliyakunnel,
1223 S., de Gouw, J. A., Graus, M., Hu, L., Koss, A., Lee, B. H., Lopez-Hilfiker, F. D., Neuman, J. A.,
1224 Paulot, F., Peischl, J., Pollack, I. B., Ryerson, T. B., Warneke, C., Williams, B. J., and Xu, J.: A large
1225 and ubiquitous source of atmospheric formic acid, Atmos. Chem. Phys., 15, 6283–6304,
1226 https://doi.org/10.5194/acp-15-6283-2015, 2015.

1227 Mohr, C., Lopez-Hilfiker, F. D., Yli-Juuti, T., Heitto, A., Lutz, A., Hallquist, M., D'Ambro, E. L.,
1228 Rissanen, M. P., Hao, L., Schobesberger, S., Kulmala, M., Mauldin III, R. L., Makkonen, U., Sipilä, M.,
1229 Petäjä, T., and Thornton, J. A.: Ambient observations of dimers from terpene oxidation in the gas
1230 phase: Implications for new particle formation and growth, Geophysical Research Letters, 44, 2958–
1231 2966, https://doi.org/10.1002/2017GL072718, 2017.

1232 Mohr, C., Thornton, J. A., Heitto, A., Lopez-Hilfiker, F. D., Lutz, A., Riipinen, I., Hong, J., Donahue, N.
1233 M., Hallquist, M., Petäjä, T., Kulmala, M., and Yli-Juuti, T.: Molecular identification of organic vapors
1234 driving atmospheric nanoparticle growth, Nat Commun, 10, 4442, https://doi.org/10.1038/s41467-019-
1235 12473-2, 2019.

1236 Mulcahy, J. P., Johnson, C., Jones, C. G., Povey, A. C., Scott, C. E., Sellar, A., Turnock, S. T.,
1237 Woodhouse, M. T., Abraham, N. L., Andrews, M. B., Bellouin, N., Browse, J., Carslaw, K. S., Dalvi,
1238 M., Folberth, G. A., Glover, M., Grosvenor, D. P., Hardacre, C., Hill, R., Johnson, B., Jones, A.,
1239 Kipling, Z., Mann, G., Mollard, J., O'Connor, F. M., Palmiéri, J., Reddington, C., Rumbold, S. T.,
1240 Richardson, M., Schutgens, N. A. J., Stier, P., Stringer, M., Tang, Y., Walton, J., Woodward, S., and
1241 Yool, A.: Description and evaluation of aerosol in UKESM1 and HadGEM3-GC3.1 CMIP6 historical
1242 simulations, Geosci. Model Dev., 13, 6383–6423, https://doi.org/10.5194/gmd-13-6383-2020, 2020.

1243 Murphy, B. N., Julin, J., Riipinen, I., and Ekman, A. M. L.: Organic aerosol processing in tropical deep
1244 convective clouds: Development of a new model (CRM-ORG) and implications for sources of particle
1245 number, Journal of Geophysical Research: Atmospheres, 120, 10,441-10,464,
1246 https://doi.org/10.1002/2015JD023551, 2015.

1247 Ng, N. L., Herndon, S. C., Trimborn, A., Canagaratna, M. R., Croteau, P. L., Onasch, T. B., Sueper,
1248 D., Worsnop, D. R., Zhang, Q., Sun, Y. L., and Jayne, J. T.: An Aerosol Chemical Speciation Monitor
1249 (ACSM) for Routine Monitoring of the Composition and Mass Concentrations of Ambient Aerosol,
1250 Aerosol Science and Technology, 45, 780–794, https://doi.org/10.1080/02786826.2011.560211,
1251 2011.

1252 Nieminen, T., Asmi, A., Maso, M. D., Aalto, P. P., Keronen, P., Petäjä, T., Kulmala, M., and Kerminen,
1253 V.-M.: Trends in atmospheric new-particle formation: 16 years of observations in a boreal-forest
1254 environment, Boreal Environ. Res., 19, 191–214, 2014.

1255 NIST Chemistry WebBook: https://webbook.nist.gov/cgi/cbook.cgi?ID=C64186&Mask=4, last access:
1256 8 November 2022.

1257 Ovadnevaite, J., Zuend, A., Laaksonen, A., Sanchez, K. J., Roberts, G., Ceburnis, D., Decesari, S.,
1258 Rinaldi, M., Hodas, N., Facchini, M. C., Seinfeld, J. H., and O' Dowd, C.: Surface tension prevails over

1259   solute effect in organic-influenced cloud droplet activation, Nature, 546, 637–641,
1260   https://doi.org/10.1038/nature22806, 2017.

1261   Paasonen, P., Asmi, A., Petäjä, T., Kajos, M. K., Äijälä, M., Junninen, H., Holst, T., Abbatt, J. P. D.,
1262   Arneth, A., Birmili, W., van der Gon, H. D., Hamed, A., Hoffer, A., Laakso, L., Laaksonen, A., Richard
1263   Leaitch, W., Plass-Dülmer, C., Pryor, S. C., Räisänen, P., Swietlicki, E., Wiedensohler, A., Worsnop,
1264   D. R., Kerminen, V.-M., and Kulmala, M.: Warming-induced increase in aerosol number concentration
1265   likely to moderate climate change, Nature Geosci, 6, 438–442, https://doi.org/10.1038/ngeo1800,
1266   2013.

1267   Paramonov, M., Aalto, P. P., Asmi, A., Prisle, N., Kerminen, V.-M., Kulmala, M., and Petäjä, T.: The
1268   analysis of size-segregated cloud condensation nuclei counter (CCNC) data and its implications for
1269   cloud droplet activation, Atmos. Chem. Phys., 13, 10285–10301, https://doi.org/10.5194/acp-13-
1270   10285-2013, 2013.

1271   Paramonov, M., Kerminen, V.-M., Gysel, M., Aalto, P. P., Andreae, M. O., Asmi, E., Baltensperger, U.,
1272   Bougiatioti, A., Brus, D., Frank, G. P., Good, N., Gunthe, S. S., Hao, L., Irwin, M., Jaatinen, A.,
1273   Jurányi, Z., King, S. M., Kortelainen, A., Kristensson, A., Lihavainen, H., Kulmala, M., Lohmann, U.,
1274   Martin, S. T., McFiggans, G., Mihalopoulos, N., Nenes, A., O'Dowd, C. D., Ovadnevaite, J., Petäjä, T.,
1275   Pöschl, U., Roberts, G. C., Rose, D., Svenningsson, B., Swietlicki, E., Weingartner, E., Whitehead, J.,
1276   Wiedensohler, A., Wittbom, C., and Sierau, B.: A synthesis of cloud condensation nuclei counter
1277   (CCNC) measurements within the EUCAARI network, Atmospheric Chemistry and Physics, 15,
1278   12211–12229, https://doi.org/10.5194/acp-15-12211-2015, 2015.

1279   Partridge, D. G., Vrugt, J. A., Tunved, P., Ekman, A. M. L., Gorea, D., and Sorooshian, A.: Inverse
1280   modeling of cloud-aerosol interactions – Part 1: Detailed response surface analysis, Atmos. Chem.
1281   Phys., 11, 7269–7287, https://doi.org/10.5194/acp-11-7269-2011, 2011.

1282   Partridge, D. G., Vrugt, J. A., Tunved, P., Ekman, A. M. L., Struthers, H., and Sorooshian, A.: Inverse
1283   modelling of cloud-aerosol interactions – Part 2: Sensitivity tests on liquid phase clouds using a
1284   Markov chain Monte Carlo based simulation approach, Atmos. Chem. Phys., 12, 2823–2847,
1285   https://doi.org/10.5194/acp-12-2823-2012, 2012.

1286   Petäjä, T., O'Connor, E. J., Moisseev, D., Sinclair, V. A., Manninen, A. J., Väänänen, R., Lerber, A.
1287   von, Thornton, J. A., Nicoll, K., Petersen, W., Chandrasekar, V., Smith, J. N., Winkler, P. M., Krüger,
1288   O., Hakola, H., Timonen, H., Brus, D., Laurila, T., Asmi, E., Riekkola, M.-L., Mona, L., Massoli, P.,
1289   Engelmann, R., Komppula, M., Wang, J., Kuang, C., Bäck, J., Virtanen, A., Levula, J., Ritsche, M.,
1290   and Hickmon, N.: BAECC: A Field Campaign to Elucidate the Impact of Biogenic Aerosols on Clouds
1291   and Climate, Bulletin of the American Meteorological Society, 97, 1909–1928,
1292   https://doi.org/10.1175/BAMS-D-14-00199.1, 2016.

1293   Petäjä, T., Tabakova, K., Manninen, A., Ezhova, E., O'Connor, E., Moisseev, D., Sinclair, V. A.,
1294   Backman, J., Levula, J., Luoma, K., Virkkula, A., Paramonov, M., Räty, M., Äijälä, M., Heikkinen, L.,
1295   Ehn, M., Sipilä, M., Yli-Juuti, T., Virtanen, A., Ritsche, M., Hickmon, N., Pulik, G., Rosenfeld, D.,
1296   Worsnop, D. R., Bäck, J., Kulmala, M., and Kerminen, V.-M.: Influence of biogenic emissions from
1297   boreal forests on aerosol–cloud interactions, Nat. Geosci., 15, 42–47, https://doi.org/10.1038/s41561-
1298   021-00876-0, 2022.

1299   Presto, A. A. and Donahue, N. M.: Investigation of α-Pinene + Ozone Secondary Organic Aerosol
1300   Formation at Low Total Aerosol Mass, Environ. Sci. Technol., 40, 3536–3543,
1301   https://doi.org/10.1021/es052203z, 2006.

1302   Pruppacher, H. R. and Klett, J. D.: Microphysics of Clouds and Precipitation, Springer Netherlands,
1303   Dordrecht, https://doi.org/10.1007/978-0-306-48100-0, 1997.

1304   Ridley, J. K., Blockley, E. W., Keen, A. B., Rae, J. G. L., West, A. E., and Schroeder, D.: The sea ice
1305   model component of HadGEM3-GC3.1, Geoscientific Model Development, 11, 713–723,
1306   https://doi.org/10.5194/gmd-11-713-2018, 2018.

1307   Robinson, A. L., Donahue, N. M., Shrivastava, M. K., Weitkamp, E. A., Sage, A. M., Grieshop, A. P.,
1308   Lane, T. E., Pierce, J. R., and Pandis, S. N.: Rethinking Organic Aerosols: Semivolatile Emissions
1309   and Photochemical Aging, Science, 315, 1259–1262, https://doi.org/10.1126/science.1133061, 2007.

1310   Roelofs, G. J. H.: Drop size dependent sulfate distribution in a growing cloud, J Atmos Chem, 14,
1311   109–118, https://doi.org/10.1007/BF00115227, 1992.

1312   Roelofs, G.-J. and Jongen, S.: A model study of the influence of aerosol size and chemical properties
1313   on precipitation formation in warm clouds, J. Geophys. Res., 109,
1314   https://doi.org/10.1029/2004JD004779, 2004.

1315   Romakkaniemi, S., Kokkola, H., and Laaksonen, A.: Parameterization of the nitric acid effect on CCN
1316   activation, Atmospheric Chemistry and Physics, 5, 879–885, https://doi.org/10.5194/acp-5-879-2005,
1317   2005.

1318   Ruehl, C. R., Chuang, P. Y., Nenes, A., Cappa, C. D., Kolesar, K. R., and Goldstein, A. H.: Strong
1319   evidence of surface tension reduction in microscopic aqueous droplets, Geophysical Research
1320   Letters, 39, https://doi.org/10.1029/2012GL053706, 2012.

1321   Ruehl, C. R., Davies, J. F., and Wilson, K. R.: An interfacial mechanism for cloud droplet formation on
1322   organic aerosols, Science, 351, 1447–1450, https://doi.org/10.1126/science.aad4889, 2016.

1323   Schobesberger, S., Lopez-Hilfiker, F. D., Taipale, D., Millet, D. B., D'Ambro, E. L., Rantala, P.,
1324   Mammarella, I., Zhou, P., Wolfe, G. M., Lee, B. H., Boy, M., and Thornton, J. A.: High upward fluxes
1325   of formic acid from a boreal forest canopy, Geophysical Research Letters, 43, 9342–9351,
1326   https://doi.org/10.1002/2016GL069599, 2016.

1327   Scott, C. E., Arnold, S. R., Monks, S. A., Asmi, A., Paasonen, P., and Spracklen, D. V.: Substantial
1328   large-scale feedbacks between natural aerosols and climate, Nature Geosci, 11, 44–48,
1329   https://doi.org/10.1038/s41561-017-0020-5, 2018.

1330   Sellar, A. A., Jones, C. G., Mulcahy, J. P., Tang, Y., Yool, A., Wiltshire, A., O'Connor, F. M., Stringer,
1331   M., Hill, R., Palmieri, J., Woodward, S., de Mora, L., Kuhlbrodt, T., Rumbold, S. T., Kelley, D. I., Ellis,
1332   R., Johnson, C. E., Walton, J., Abraham, N. L., Andrews, M. B., Andrews, T., Archibald, A. T.,
1333   Berthou, S., Burke, E., Blockley, E., Carslaw, K., Dalvi, M., Edwards, J., Folberth, G. A., Gedney, N.,
1334   Griffiths, P. T., Harper, A. B., Hendry, M. A., Hewitt, A. J., Johnson, B., Jones, A., Jones, C. D.,
1335   Keeble, J., Liddicoat, S., Morgenstern, O., Parker, R. J., Predoi, V., Robertson, E., Siahaan, A.,
1336   Smith, R. S., Swaminathan, R., Woodhouse, M. T., Zeng, G., and Zerroukat, M.: UKESM1:
1337   Description and Evaluation of the U.K. Earth System Model, Journal of Advances in Modeling Earth
1338   Systems, 11, 4513–4558, https://doi.org/10.1029/2019MS001739, 2019.

1339   Sellar, A. A., Walton, J., Jones, C. G., Wood, R., Abraham, N. L., Andrejczuk, M., Andrews, M. B.,
1340   Andrews, T., Archibald, A. T., de Mora, L., Dyson, H., Elkington, M., Ellis, R., Florek, P., Good, P.,
1341   Gohar, L., Haddad, S., Hardiman, S. C., Hogan, E., Iwi, A., Jones, C. D., Johnson, B., Kelley, D. I.,
1342   Kettleborough, J., Knight, J. R., Köhler, M. O., Kuhlbrodt, T., Liddicoat, S., Linova-Pavlova, I.,
1343   Mizielinski, M. S., Morgenstern, O., Mulcahy, J., Neininger, E., O'Connor, F. M., Petrie, R., Ridley, J.,
1344   Rioual, J.-C., Roberts, M., Robertson, E., Rumbold, S., Seddon, J., Shepherd, H., Shim, S.,
1345   Stephens, A., Teixiera, J. C., Tang, Y., Williams, J., Wiltshire, A., and Griffiths, P. T.: Implementation
1346   of U.K. Earth System Models for CMIP6, Journal of Advances in Modeling Earth Systems, 12,
1347   e2019MS001946, https://doi.org/10.1029/2019MS001946, 2020.

1348   Shrivastava, M., Cappa, C. D., Fan, J., Goldstein, A. H., Guenther, A. B., Jimenez, J. L., Kuang, C.,
1349   Laskin, A., Martin, S. T., Ng, N. L., Petaja, T., Pierce, J. R., Rasch, P. J., Roldin, P., Seinfeld, J. H.,
1350   Shilling, J., Smith, J. N., Thornton, J. A., Volkamer, R., Wang, J., Worsnop, D. R., Zaveri, R. A.,
1351   Zelenyuk, A., and Zhang, Q.: Recent advances in understanding secondary organic aerosol:
1352   Implications for global climate forcing, Reviews of Geophysics, 55, 509–559,
1353   https://doi.org/10.1002/2016RG000540, 2017.

1354   Sihto, S.-L., Mikkilä, J., Vanhanen, J., Ehn, M., Liao, L., Lehtipalo, K., Aalto, P. P., Duplissy, J.,
1355   Petäjä, T., Kerminen, V.-M., Boy, M., and Kulmala, M.: Seasonal variation of CCN concentrations and

1356   aerosol activation properties in boreal forest, Atmospheric Chemistry and Physics, 11, 13269–13285,
1357   https://doi.org/10.5194/acp-11-13269-2011, 2011.

1358   Sorjamaa, R., Svenningsson, B., Raatikainen, T., Henning, S., Bilde, M., and Laaksonen, A.: The role
1359   of surfactants in Köhler theory reconsidered, Atmospheric Chemistry and Physics, 4, 2107–2117,
1360   https://doi.org/10.5194/acp-4-2107-2004, 2004.

1361   Sporre, M. K., Blichner, S. M., Karset, I. H. H., Makkonen, R., and Berntsen, T. K.: BVOC–aerosol–
1362   climate feedbacks investigated using NorESM, Atmospheric Chemistry and Physics, 19, 4763–4782,
1363   https://doi.org/10.5194/acp-19-4763-2019, 2019.

1364   Sporre, M. K., Blichner, S. M., Schrödner, R., Karset, I. H. H., Berntsen, T. K., van Noije, T., Bergman,
1365   T., O'Donnell, D., and Makkonen, R.: Large difference in aerosol radiative effects from BVOC-SOA
1366   treatment in three Earth system models, Atmospheric Chemistry and Physics, 20, 8953–8973,
1367   https://doi.org/10.5194/acp-20-8953-2020, 2020.

1368   Spracklen, D. V., Bonn, B., and Carslaw, K. S.: Boreal forests, aerosols and the impacts on clouds
1369   and climate, Philosophical Transactions of the Royal Society A: Mathematical, Physical and
1370   Engineering Sciences, 366, 4613–4626, https://doi.org/10.1098/rsta.2008.0201, 2008.

1371   Storkey, D., Blaker, A. T., Mathiot, P., Megann, A., Aksenov, Y., Blockley, E. W., Calvert, D., Graham,
1372   T., Hewitt, H. T., Hyder, P., Kuhlbrodt, T., Rae, J. G. L., and Sinha, B.: UK Global Ocean GO6 and
1373   GO7: a traceable hierarchy of model resolutions, Geoscientific Model Development, 11, 3187–3213,
1374   https://doi.org/10.5194/gmd-11-3187-2018, 2018.

1375   Thornhill, G., Collins, W., Olivié, D., Skeie, R. B., Archibald, A., Bauer, S., Checa-Garcia, R., Fiedler,
1376   S., Folberth, G., Gjermundsen, A., Horowitz, L., Lamarque, J.-F., Michou, M., Mulcahy, J., Nabat, P.,
1377   Naik, V., O'Connor, F. M., Paulot, F., Schulz, M., Scott, C. E., Séférian, R., Smith, C., Takemura, T.,
1378   Tilmes, S., Tsigaridis, K., and Weber, J.: Climate-driven chemistry and aerosol feedbacks in CMIP6
1379   Earth system models, Atmospheric Chemistry and Physics, 21, 1105–1126,
1380   https://doi.org/10.5194/acp-21-1105-2021, 2021.

1381   Thornton, J. A., Mohr, C., Schobesberger, S., D'Ambro, E. L., Lee, B. H., and Lopez-Hilfiker, F. D.:
1382   Evaluating Organic Aerosol Sources and Evolution with a Combined Molecular Composition and
1383   Volatility Framework Using the Filter Inlet for Gases and Aerosols (FIGAERO), Acc. Chem. Res., 53,
1384   1415–1426, https://doi.org/10.1021/acs.accounts.0c00259, 2020.

1385   Topping, D., Connolly, P., and McFiggans, G.: Cloud droplet number enhanced by co-condensation of
1386   organic vapours, Nature Geosci, 6, 443–446, https://doi.org/10.1038/ngeo1809, 2013.

1387   Topping, D. O. and McFiggans, G.: Tight coupling of particle size, number and composition in
1388   atmospheric cloud droplet activation, Atmospheric Chemistry and Physics, 12, 3253–3260,
1389   https://doi.org/10.5194/acp-12-3253-2012, 2012.

1390   Tunved, P., Hansson, H.-C., Kerminen, V.-M., Ström, J., Maso, M. D., Lihavainen, H., Viisanen, Y.,
1391   Aalto, P. P., Komppula, M., and Kulmala, M.: High Natural Aerosol Loading over Boreal Forests,
1392   Science, 312, 261–263, https://doi.org/10.1126/science.1123052, 2006.

1393   Turnock, S. T., Allen, R. J., Andrews, M., Bauer, S. E., Deushi, M., Emmons, L., Good, P., Horowitz,
1394   L., John, J. G., Michou, M., Nabat, P., Naik, V., Neubauer, D., O'Connor, F. M., Olivié, D., Oshima, N.,
1395   Schulz, M., Sellar, A., Shim, S., Takemura, T., Tilmes, S., Tsigaridis, K., Wu, T., and Zhang, J.:
1396   Historical and future changes in air pollutants from CMIP6 models, Atmospheric Chemistry and
1397   Physics, 20, 14547–14579, https://doi.org/10.5194/acp-20-14547-2020, 2020.

1398   Twomey, S.: Pollution and the planetary albedo, Atmospheric Environment (1967), 8, 1251–1256,
1399   https://doi.org/10.1016/0004-6981(74)90004-3, 1974.

1400   Twomey, S.: The Influence of Pollution on the Shortwave Albedo of Clouds, Journal of the
1401   Atmospheric Sciences, 34, 1149–1152, https://doi.org/10.1175/1520-
1402   0469(1977)034<1149:TIOPOT>2.0.CO;2, 1977.

1403 Uusitalo, H., Kontkanen, J., Ylivinkka, I., Ezhova, E., Demakova, A., Arshinov, M., Belan, B. D.,
1404 Davydov, D., Ma, N., Petäjä, T., Wiedensohler, A., Kulmala, M., and Nieminen, T.: Occurrence of new
1405 particle formation events in Siberian and Finnish boreal forest, Aerosols/Field
1406 Measurements/Troposphere/Physics (physical properties and processes), https://doi.org/10.5194/acp-
1407 2021-530, 2021.

1408 Vehkamäki, H., Kulmala, M., Napari, I., Lehtinen, K. E. J., Timmreck, C., Noppel, M., and Laaksonen,
1409 A.: An improved parameterization for sulfuric acid–water nucleation rates for tropospheric and
1410 stratospheric conditions, Journal of Geophysical Research: Atmospheres, 107, AAC 3-1-AAC 3-10,
1411 https://doi.org/10.1029/2002JD002184, 2002.

1412 Walters, D., Boutle, I., Brooks, M., Melvin, T., Stratton, R., Vosper, S., Wells, H., Williams, K., Wood,
1413 N., Allen, T., Bushell, A., Copsey, D., Earnshaw, P., Edwards, J., Gross, M., Hardiman, S., Harris, C.,
1414 Heming, J., Klingaman, N., Levine, R., Manners, J., Martin, G., Milton, S., Mittermaier, M., Morcrette,
1415 C., Riddick, T., Roberts, M., Sanchez, C., Selwood, P., Stirling, A., Smith, C., Suri, D., Tennant, W.,
1416 Vidale, P. L., Wilkinson, J., Willett, M., Woolnough, S., and Xavier, P.: The Met Office Unified Model
1417 Global Atmosphere 6.0/6.1 and JULES Global Land 6.0/6.1 configurations, Geoscientific Model
1418 Development, 10, 1487–1520, https://doi.org/10.5194/gmd-10-1487-2017, 2017.

1419 Wiedensohler, A., Ma, N., Birmili, W., Heintzenberg, J., Ditas, F., Andreae, M. O., and Panov, A.:
1420 Infrequent new particle formation over the remote boreal forest of Siberia, Atmospheric Environment,
1421 200, 167–169, https://doi.org/10.1016/j.atmosenv.2018.12.013, 2019.

1422 Williams, J., Crowley, J., Fischer, H., Harder, H., Martinez, M., Petäjä, T., Rinne, J., Bäck, J., Boy, M.,
1423 Dal Maso, M., Hakala, J., Kajos, M., Keronen, P., Rantala, P., Aalto, J., Aaltonen, H., Paatero, J.,
1424 Vesala, T., Hakola, H., Levula, J., Pohja, T., Herrmann, F., Auld, J., Mesarchaki, E., Song, W.,
1425 Yassaa, N., Nölscher, A., Johnson, A. M., Custer, T., Sinha, V., Thieser, J., Pouvesle, N., Taraborrelli,
1426 D., Tang, M. J., Bozem, H., Hosaynali-Beygi, Z., Axinte, R., Oswald, R., Novelli, A., Kubistin, D.,
1427 Hens, K., Javed, U., Trawny, K., Breitenberger, C., Hidalgo, P. J., Ebben, C. J., Geiger, F. M.,
1428 Corrigan, A. L., Russell, L. M., Ouwersloot, H. G., Vilà-Guerau de Arellano, J., Ganzeveld, L., Vogel,
1429 A., Beck, M., Bayerle, A., Kampf, C. J., Bertelmann, M., Köllner, F., Hoffmann, T., Valverde, J.,
1430 González, D., Riekkola, M.-L., Kulmala, M., and Lelieveld, J.: The summertime Boreal forest field
1431 measurement intensive (HUMPPA-COPEC-2010): an overview of meteorological and chemical
1432 influences, Atmos. Chem. Phys., 11, 10599–10618, https://doi.org/10.5194/acp-11-10599-2011, 2011.

1433 Yan, C., Nie, W., Äijälä, M., Rissanen, M. P., Canagaratna, M. R., Massoli, P., Junninen, H., Jokinen,
1434 T., Sarnela, N., Häme, S. A. K., Schobesberger, S., Canonaco, F., Yao, L., Prévôt, A. S. H., Petäjä,
1435 T., Kulmala, M., Sipilä, M., Worsnop, D. R., and Ehn, M.: Source characterization of highly oxidized
1436 multifunctional compounds in a boreal forest environment using positive matrix factorization, Atmos.
1437 Chem. Phys., 16, 12715–12731, https://doi.org/10.5194/acp-16-12715-2016, 2016.

1438 Yatavelli, R. L. N., Mohr, C., Stark, H., Day, D. A., Thompson, S. L., Lopez-Hilfiker, F. D.,
1439 Campuzano-Jost, P., Palm, B. B., Vogel, A. L., Hoffmann, T., Heikkinen, L., Äijälä, M., Ng, N. L.,
1440 Kimmel, J. R., Canagaratna, M. R., Ehn, M., Junninen, H., Cubison, M. J., Petäjä, T., Kulmala, M.,
1441 Jayne, J. T., Worsnop, D. R., and Jimenez, J. L.: Estimating the contribution of organic acids to
1442 northern hemispheric continental organic aerosol, Geophysical Research Letters, 42, 6084–6090,
1443 https://doi.org/10.1002/2015GL064650, 2015.

1444 Yli-Juuti, T., Mielonen, T., Heikkinen, L., Arola, A., Ehn, M., Isokääntä, S., Keskinen, H.-M., Kulmala,
1445 M., Laakso, A., Lipponen, A., Luoma, K., Mikkonen, S., Nieminen, T., Paasonen, P., Petäjä, T.,
1446 Romakkaniemi, S., Tonttila, J., Kokkola, H., and Virtanen, A.: Significance of the organic aerosol
1447 driven climate feedback in the boreal area, Nat Commun, 12, 5637, https://doi.org/10.1038/s41467-
1448 021-25850-7, 2021.

1449 Zhang, Y., Peräkylä, O., Yan, C., Heikkinen, L., Äijälä, M., Daellenbach, K. R., Zha, Q., Riva, M.,
1450 Garmash, O., Junninen, H., Paatero, P., Worsnop, D., and Ehn, M.: Insights into atmospheric
1451 oxidation processes by performing factor analyses on subranges of mass spectra, Atmos. Chem.
1452 Phys., 20, 5945–5961, https://doi.org/10.5194/acp-20-5945-2020, 2020.

1453